# Permafrost degradation in a changing climate: Evolution of the Batagay megaslump

**Ksenia Winter**

2026
Department of
Earth and Environmental Sciences
Lund University
Sölvegatan 12
S-223 62 Lund
Sweden

Ksenia Winter (2026).
***Permafrost degradation in a changing climate: Evolution of the Batagay megaslump (English)***.
***Upptining av permafrost under klimatförändring: Utvecklingen av Batagay-megaslumpen (Swedish).***
Bachelor degree thesis, 15 credits in Physical Geography and Ecosystem Science
Department of Earth and Environmental Sciences, Lund University

Level: Bachelor of Science (BSc)

Course duration: *March* 2026 until *June* 2026

Disclaimer

# Permafrost degradation in a changing climate:
# Evolution of the Batagay megaslump

---

Ksenia Winter

Bachelor thesis, 15 credits, in Physical Geography and Ecosystem Analysis

Supervisor:
Harry Lankreijer
Department of Earth and Environmental Sciences,
Lund University

Examiner:
Karin Hall
Department of Earth and Environmental Sciences,
Lund University

Acknowledgements

I would like to thank my supervisor Harry Lankreijer for his guidance and insightful feedback throughout this thesis. I would also like to thank my family who supported me and shared my interest for this fascinating topic.

Abstract

The Arctic is warming rapidly leading to the development of new thermokarst landscape features. Among the most rapidly developing landforms are retrogressive thaw slumps. The largest known thaw slump is the Batagay megaslump located in the Sakha republic, Russia. This thesis aims to assess the thaw slumps growth' and yearly retreat rates through systematic digitization of openly accessible satellite imagery sourced from Copernicus and USGS, covering 1991 and the period from 1999 to 2025. Directional expansion is examined using 18 transect lines radiating from a central point in 20° increments. The mean annual expansion is calculated across all transects to assess annual growth patterns and retreat rates. Regional climate conditions and potential climate shifts are analyzed to contextualize changes in the thaw slump. Finally, the relationship between climatic drivers such as mean annual temperature, seasonal temperature, thawing degree days, annual precipitation, seasonal precipitation and the RTS' annual retreat rate is quantified. The results reveal an asymmetrical growth pattern, with larger retreat in southwestern direction. The overall rate of the RTS expansion decreases after 2010, whilst the RTS areal extend further expands. Climate analysis reveals warming trends for mean annual temperature, spring, summer and autumn, whilst winter temperatures decrease. Yearly and seasonal precipitation remain unchanged. Statistical regression analysis for the period 2002-2025 yields no significant relationships between climate variables and annual RTS retreat, with the exception for summer temperatures (Jun-Aug and May-Sept) of the preceding year.

**Keywords:** *Batagay megaslump, retrogressive thaw slump, permafrost degradation, climate change*

Table of Contents

# 1 Introduction

The Arctic is warming at a faster rate than any other region on earth due to climate change (Rantanen et al., 2022). Vast areas of the Arctic are underlain by permafrost, making up 15% of earths exposed surface in the northern hemisphere (Obu, 2021). Permafrost is defined as ground, soil or rock that has been below 0°C for at least two consecutive years (French, 2018). Permafrost occurs as sporadic, discontinuous and continuous permafrost, depending on climatic conditions and latitude, the latter's distribution increasing towards higher latitudes (Zhang et al., 2000). Permafrost requires long periods of cold conditions to form and penetrate deep into the ground (Barry & Gan, 2022). However, it can thaw rapidly in a warming climate, which can have major effects on ecosystem functions, hydrology, geomorphology and carbon and nitrogen release (Lafrenière et al., 2013, Kokelj et al., 2005).

Permafrost thaw commonly occurs through the deepening of the active layer. This is the surface layer which seasonally thaws and therefore is not frozen all year round. The depth varies depending on insulation, soil, soil water content, heat conductivity and more (Wlostowski et al., 2017). Thawing also occurs through thermal denudation processes, which are occurring mainly on slopes and involve the thawing of ice rich grounds. This leads to lowering or destruction of land surface and occur through the exposure of ground ice. This ground ice is uncovered by gravitational and erosion processes which exposes it to air temperature, solar radiation and surface runoff, thus leading to melting of the ice. Seasonal snow melt, summer precipitation can accelerate thaw process along ice wedges (Timofeev& Vtyurina, 1983; Are, 1980; Zhigarev, 1975.; French, 2018).

As permafrost degrades new landscape features emerge and alter the Arctic terrain. One of the most prominent and fast developing features are retrogressive thaw slumps (RTS). These are large depressions formed by thawing of ice rich permafrost which destabilize slopes and trigger mass wasting, which in turn exposes more ground ice (French, 2018; Burn, 2020). Their development is common in regions with ground containing high volumetric ice content or large ice bodies nearby the zone of thawing (Kizyakov, 2025). Their activity can be initiated by localized slope failures along coasts, streams or lakes. The exposed ice rich sediments continue to thaw leading to expansion of the thaw slump and headwall retreat, which is the RTSs steep upper slope, of several meters per year. As the RTS increases in size it redistributes sediment and mud from the headwall through slides, debris flow or meltwater transport (Lafrenière et al., 2013).

A region particularly affected by these processes is Siberia, in particular regions in the Sakha republic (Yakutia). Here one of the world's oldest, deepest and most ice rich permafrost can be found. Although being one of the coldest places on earth, it too has experienced temperature warming over the last decades, leading to the emergence of more thaw slumps or the growth of existing thaw slumps (Vasil'chuk and Vasil'chuk, 1997). Typically thaw slumps reach a maximum size 20 ha. However, thaw slumps that exceed this size are titled megaslumps (Lacelle et al., 2015). The largest known retrogressive thaw slump on earth is the Batagay megaslump (Murton, 2023). Therefore, yearly evolution and expansion patterns of this landscape feature are of particular interest.

## 1.1 Aim

This thesis presents the areal extend of the Batagay megaslump for1991 and over the period from 1999 to 2025 based on digitized openly assessable satellite imagery. Furthermore, both the expansion rate of the RTS and its directional growth patterns will be examined. The study analyses whether temperature and precipitation have a statistically significant relationship with yearly RTS growth rates. Additionally, it will be examined what factors contribute to the Batagay megaslump's size.

# 2 Background

## 2.1 Glaciation History and Permafrost in Yakutia

Yakutia is situated on the Siberian plateau, and is characterized by a mountainous landscape (Kizyakov et. al, 2022). In Yakutia permafrost can reach a depth of 400m or 300m as the ground has not been covered by ice sheets during the Pleistocene (French, 2018; Ohta et al., 2019). This resulting in deeper and more ice rich ground compared to North America. Only mountains and uplands were covered by ice sheets, whereas lowlands remained largely ice free, mainly due to aridity, as mountain belts as well as the Tibetan and Asian plateau prevented moisture filled winds from the pacific or Arctic Ocean (Ohta et al., 2019).

Permafrost is dependent on the balance between internal heat gain with depth and heat loss from the surface (French, 2018). The continuous permafrost ground in Yakutia not only consists of soils and rocks, but is interrupted by few tenth percent to eighty to ninety percent of ground ice (Obu, 2021).

Ground ice is not always the same and appears in different varieties. For instance, pore ice, which is widespread near the surface and in the active layer and holds soil grains together forming in capillary spaces when moisture is present (French, 2018, Mackay, 1972). Segregated ice forms few millimeters to few meters' thick lenses or layers of ice. They result from migration of pore water to the frozen fringe. Water saturated fine grained sediments are especially suitable (French, 2018, Mackay, 1972). Intrusive ice forms by the intrusion of water, usually under pressure, into the frozen zone. Meltwater from snow or summer rain freezes to into a vertical foliation or structure. Sheets of foliated ice are named ice wedges (Barry & Gan, 2022).

An area with a vast extend of ice wedges in soil is Yakutia. Here the high ice content is known as Yedoma. Specifically, it is ice-rich silty loam containing massive ice wedges which were deposited under subaerial conditions in lowlands (Barry & Gan, 2022; Schirrmeister et al. 2013; Zimov etal., 2006). Arctic and boreal permafrost store about 50 % of total terrestrial Carbon, with 25% accumulating in Yedoma (Barreto et al., 2024). To give some perspective, the vegetation carbon reservoir is 650 Gt, while in frozen Yedoma it is estimated to be about 500Gt (Barry & Gan, 2022; Zimov et. al., 2006).

## 2.2 Impact on permafrost

Vegetation and organic matter insulate the ground by reducing the interplay of heat and water exchange between the ground and atmosphere. It traps snow and shades the ground which maintains colder soil temperatures. The soil moisture, stored within the active layer, is taken up by vegetation. (French, 2018; Ohta et al., 2019). Fires however destroy the organic matter and lead to deep thawing and soil subsidence. (Ohta et al., 2019; Woo, 2012)

Snow also has an influence on local permafrost conditions, as it insulates the soil from frost penetration after heavy snowfall in late autumn and early winter. Snow persisting into late spring leads to delay of ground thawing. Additionally, fresh snow has a very high albedo, reflecting most incoming solar radiation and thereby keeping the ground and lower atmosphere cool (Woo, 2012). Vast amounts of snow can accumulate in gullies or lee slopes (French, 2018). In spring, when the snow cover melts, it can lead to a deepening of the active layer. Therefore, both the amount and timing have an impact on permafrost surface temperatures and development of active layer in the summer (Lamoureux & Lafrenière, 2009; Ling & Zhang, 2003).

## 2.3 Permafrost degradation

### 2.3.1 Active Layer

Lying above the permafrost is the active layer which freezes in winter and thaws in summer. The dynamic of the active layer is linked to permafrost degradation, as changes in climate and surface conditions lead to the downward extensions of the active layer and permafrost table, thereby melting ground ice (Kizyakov et. al., 2024). This seasonally frozen ground is less affected by diurnal and annual temperatures with increasing depth (see *Figure 1*). The effect stops completely around a depth of 10-15m (Barry & Gan, 2022). Salinity or clay content of permafrost allows for annual freezing and thawing even if temperature stays below 0° (French, 2018). Therefore, thaw depth varies with soil material. Sandy soils, present beneath Yakutia's pine forests, facilitate water percolation and thaw more quickly than soils with a high loam content (Barry & Gan, 2022).

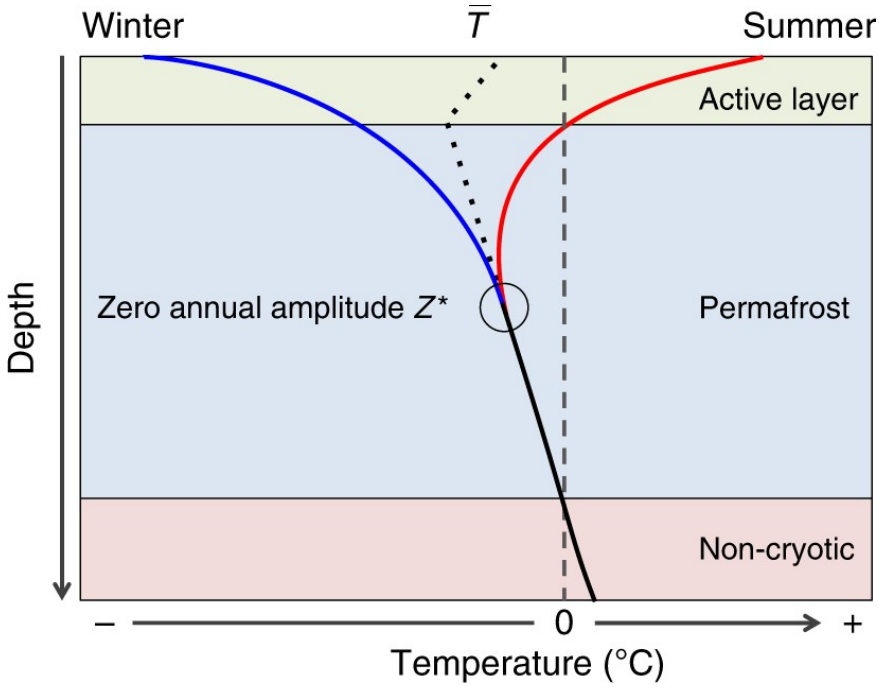


*Figure 1. Temperature profile in soil in permafrost environments during summer and winter, taken from Biskaborn et al. (2019).*

The active layer is influenced by latitude as there is a shorter thawing season, temperature, snow and vegetation cover (French, 2018). Active layer warms in spring, deepens in summer and freezes in autumn (Boike et al. 1998; Zhao et al. 2000). A shallow active layer is present in higher latitudes with shorter thawing season, lower temp and thicker vegetation and snow cover. In contrast the active layer is deeper in well drained soils (Lafrenière et al., 2013; Zhang et al., 2005). The interannual active layer development has been found to strongly correlate with the mean annual air temperature, snow depth and the seasonal thawing degree-day sum (Zhang 2005).

At the bottom of the active layer and above the upper permafrost, the transient layer is located. In years with exceptional summer warmth the active layer deepens, leading to partial thawing of this ice rich zone. This promotes slope instability and rapid mass movements. This layer forms through temperature gradients in the soil. Moisture wanders during winter upwards and downwards during summer (French, 2018; Ohta et al., 2019).

### 2. 3.2 Thermal denudation and Retrogressive thaw slumps

The destruction and lowering of the surface in permafrost regions by a wide range of relief forming processes is called thermal denudation (Timofeev & Vtyurina, 1983). Thermal denudation is initiated by seasonal thawing affecting the upper surface of substantial ground ice, where exposed frozen deposits and ground ice melt. This is through the influence of air heat, solar radiation, gravitational and erosional processes. Important hereby is the shape and volume of ground ice. Sediments previously holding ice cannot hold it anymore once thawed, leading their collapse (Are,1980; Zhigarev, 1975)

There are two types of thermal denudation, frontal and lateral. Frontal thermal denudation involves surface disturbance through external factors which impact the top layers and lead to

lowering of the surface and exposure of frozen ground (Kizyakov, 2025). However, during lateral thermal denudation permafrost erodes by abrasion often along riverbanks, seacoasts, lake shores, thaw thermocirques and on slopes. In these cases, running water such as surface runoff, from snowmelt, summer precipitation, or thawing permafrost, concentrated along ice wedges causes thawing (French, 2018).

A landscape feature emerging though thermal denudation processes in thermokarst regions, areas shaped by thawing of ice-rich permafrost or melting of ground ice, are retrogressive thaw slumps (RTS). They form in areas where permafrost contains high volumetric ice content or massive ground ice bodies subject to seasonal thawing. Their initiation is active layer detachment slides, localized slope failures, thus exposing ice to air temperature and solar radiation. The thawing in turn produces large volumes of water, this added pressure then leads to slope failure (Kizyakov, 2025).

The RTS growth is sustained by the steep headwall retreat which is composed of active layer and low ice content permafrost (see *Figure 2*). Downslope the RTS is often filled with mud and debris from meltwater and soil from the collapse of the undercut headwall. Below, vast amount of ice are contained in sediments or massive ice. As headwall retreats, falls, slides, debris flows, meltwater and sub slump melt redistribute debris (see *Figure 2*) (Lafrenière et al., 2013).

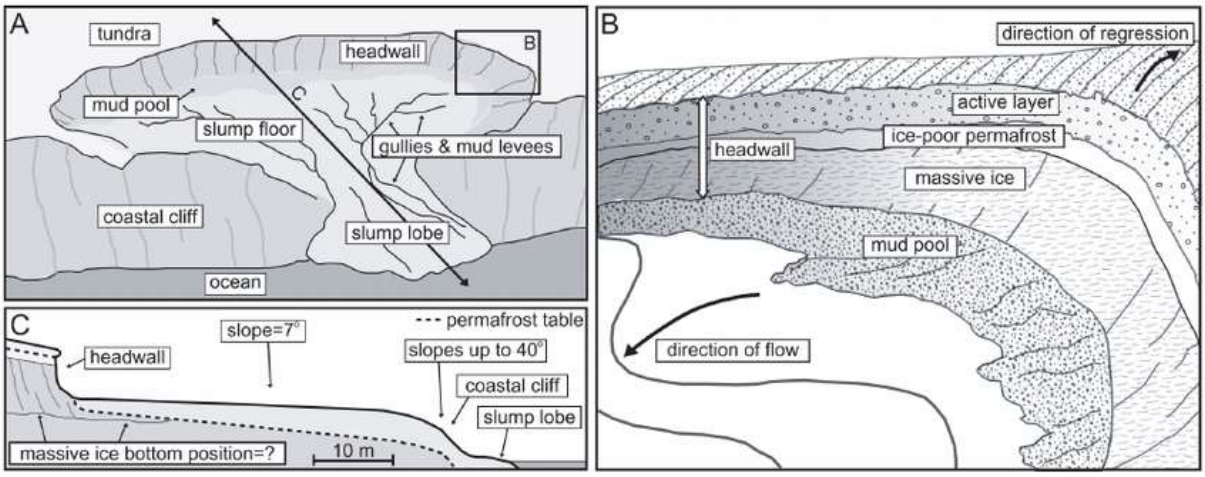


*Figure 2. Morphological components of a retrogressive thaw slump. Retrieved from Lantuit & Pollard (2005).*

# 3 Method

## 3.1 Study Site

The Batagay RTS (67°34'41.83"N, 134°45'46.91"E (Google Earth)) is located in the Sakha republic (Yakutia), eastern Russia. 10km south east to the city Batagay and within the Yana Highlands (see *Figure 1*) (Murton et al., 2017).

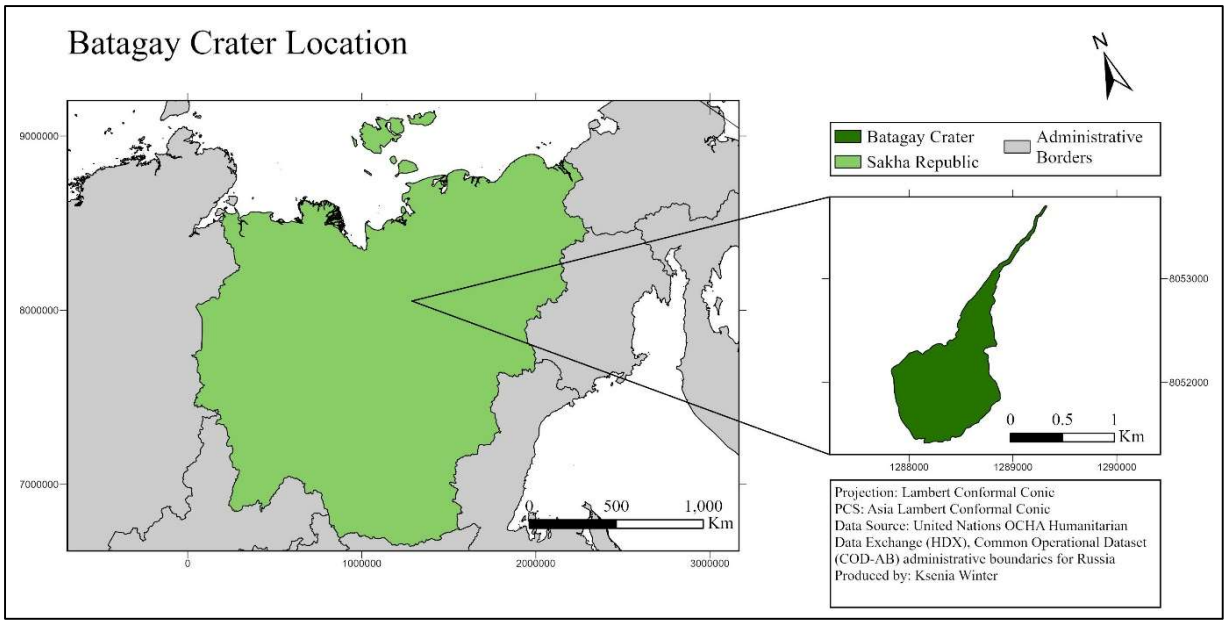


*Figure 3. Location of the Batagay RTS in the Sakha Republic (Yakutia), eastern Russia.*

The Yana Highlands are situated between the Verkhoyansk Range to the west and the Chersky Range to the east. Between the mountain ranges, the landscape is characterized by varied topography with scattered hills and mountains, gradually flattening toward the valleys of the Yana and Batagay rivers. Located on the northeastern hillslope of Mt. Khatyngnakh, at a height of about 330m, the site lies on the left bank of the Batagay River (Murton et al., 2017). Meltwater from the RTS drains northeastward, through a gully, into the Batagay River, which flows from northwest to southeast before joining the larger Yana River (see *Figure 4*). The RTS itself is situated on the southeastern side of the Yana River valley, making it part of the Yana Uplands. The Yana River flows northward and eventually drain into the Laptev Sea in the Arctic Ocean (Murton et al., 2017; Kizyakov et al., 2024).

The Batagay megaslump lies within the Arctic circle (Kizyakov et al., 2024). Being so far in the country and so high up north the region has a continental climate, characterized by large differences between the winter and summer months (Opel et al., 2019). The region's long winters and short summers and continental climate make it one of the coldest places on earth, located within the cold belt (Pražnikar, 2016). Mean temperatures can reach up to 16°C in summer and –42°C in winter (ERA5-Land). Precipitation in the Sakha republic is scarce with an average of 279.26 mm per year (ERA5-Land). During winter snow accumulates within the RTS on the slump floor (Murton et. al., 2023).

These cold temperatures have promoted and maintained the extend and depth of permafrost in the region. Large syngenetic ice wedges have formed, while sediments accumulated (Yedoma), making the Batagay area susceptible to thaw and thermokarst processes (Woo, 2012). The megaslump has headwalls reaching up to 55m to the southwest and an outflow towards the northeast (Murton et. al., 2017).

The soil distribution in the RTS is not uniform, rather there is a yellowish gray fine sand within the active layer and beneath ice rich sandy deposits (Murton et.al., 2017; Opel et.al, 2026).

Below the permafrost sediment layer (Yedoma), bedrock of turrasic siltstone and soapstone is found. Betrock in the Batagay RTS floor shows in meltwater channels (Murton et.al., 2017; Opel et.al, 2026). Around the RTS the vegetation is open woodland as the area is situated in the taiga landscape in the boreal forest zone (Murton et al., 2017). The dominant species are larch (*Larix cajanderi*) leaving the forest quite open. Small and low trees such as common birch, alder, and Siberian dwarf pine occur also. The ground layer is covered by lichen and moss. Whitin the Batagay RTS itself there are signs of early succession (Vadakkedath, 2020).

*Figure 4. Batagay megaslump, looking upslope (southwestward), in summer 2015. Photograph taken by A. Gabyshev and retrieved from Murton et.al., (2023).*

### 3.1.1 Batagay thaw slump initiation

The Batagay RTS developed initially through anthropogenic influence (and grew more in size through changes in climate.) An existing hillslope gully widened after the disturbance of vegetation cover through logging activity. This disturbed the insulation properties of vegetation leading to precipitation and solar radiation penetrating to the soil surface. Tracked vehicles further destabilized the vegetation cover and soil (Kunitsky et al., 2013). This gully was widened and deepened. In the 1980s the gully transitioned into a bowl shaped RTS after erosion reached ice rich permafrost and was further shaped by lateral thermal denudation processes (Woo, 2012).

### 3.1.2 Comparison to other Retrogressive thaw slumps

RTS are found in the northern hemisphere in permafrost regions of north western Canada, China, particularly the Qinghai-Tibetan Plateau and the Qilian Mountains, and the US, northern Alaska. Here thaw slumps do not grow as deep or wide, because, unlike in Siberia, these regions were covered by ice sheets during the Pleistocene. This led to the frost not being able penetrate

as deeply into the soil, resulting in less available ice for thawing. Additionally, their growth can be self-limiting if moisture is unavailable to redeposit debris and mud, covering underlying ice (Leibman et al., 2023, Makopoulou et al., 2024, Ward Jones et. al., 2019).

## 3.2 Data and Data processing

The data described in this section was processed in ArcGIS Pro (Version 3.6.0) and Microsoft Excel (Version 2508). For full reference of the data used and described see Appendix *Table A1*.

To be able to analyze and estimate the Batagay thaw slump growth, satellite images from Sentinel 2 were used at 10m resolution (see Appendix *Table A2, Figure A4, Figure A5*). These were downloaded from Copernicus browser. Images were available from 2016 to 2025, with 2016 being the oldest possible year for Sentinel 2. Although this timescale also shows growth of the RTS, it was more insightful to cover a larger time scale to analyze and identify the rate of change. Therefore, older images from 1991, 1999 to 2015 were used from a different data source, namely Landsat 8 from USGS at a 30m resolution (see Appendix *Table A1, Figure A1, Figure A2, Figure A3*).

Satellite images were chosen based on visibility and cloud cover. To ensure that the RTS was greatly visible and its boundaries were not obscured by clouds or their shade, cloud cover was filtered to be at a maximum of 30%, as this was the minimum cloud cover possible in the Copernicus browser website and 0% in USGS, which had to be increased if there were no suitable images. The images were controlled so clouds were not over the study area. As the study area is not that big it was usually fine if clouds were in the image as long as they were not covering the RTS.

Images were selected to be in August. This is due to the snow covering the area for most of the year but it being melted during that period. At this stage the RTS had most likely already reached its grow potential for that year. This was not always possible due to bad image quality or cloud cover, therefore moths like July and June or even May were selected. A full list of satellite images used for digitizing are linked in the appendix with the date and source (see appendix *Table A2*). They were already in the correct coordinate system WGS 1984 UTM Zone 53N, no further processing had to be carried out.

The Digital elevation model (DEM) has a resolution of 2m and was retrieved from Arctic DEM through Google earth engine. To download this data a code was generated with the assistance of AI (Claude Code). In ArcGIS pro this layer was projected into WGS 1984 UTM Zone 53N. It was further processed into a slope layer and hill shade layer.

Climate data was initially taken from the Verkhoyansk meteorological station which is located about 50km south west from the Batagay RTS, situated to the east of the Verkhoyansk range. It is assumed that the temperature and precipitation data is representative and similar to the study area. The station is located at an elevation of 138m, and the temperature sensor is located 2m above ground. Temperature readings were available with a three-hour interval for each day.

Due to inconsistency of the weather station data, which had changes in instruments in 2010, satellite inferred climatic data was chosen. For a complete dataset over the study period from 1999 to 2025 climate data from Era5-Land (Copernicus, Muñoz Sabater, 2021) was used to get monthly mean temperature and precipitation monthly sum, as well as daily mean temperature. This dataset is derived from 9km satellite data averaging, 2m above ground. Both the Copernicus ERA-Land and Verkhoyansk meteorological station cover a longer measurement period, namely from 1981 to 2025. To see better and more accurate temperature trends in the region, for the calculation itself climate data from 2002 to 2025 was selected. These were downloaded from Google earth engine using a code written with the help of an AI tool (Claude Code).

## 3.3 Methodology

### 3.3.1 Digitizing

Using satellite images, the Batagay thaw slump area could be identified and its boundary traced in order to create a RTS extend polygon in ArcGIS Pro. The RTS boundary was manually traced with a set topology rule that previous year will not exceed the following year. To keep the digitization consistent only boundaries where there is a clear edge were traced. The inner side of the shadow was traced. Whilst digitizing scale was 1:9000 for 10m resolution image and 15000 for 30m resolution image to identify RTS boundaries, but not to trace pixel noise.

The following order was kept throughout digitization; True color band arrangement, to look at the RTS extend and general shape. Afterwards the band order was changed to a false color composite in order to incorporate the NIR band. This was done to see a greater difference between vegetation and the bare soil.

To better identify RTS boundary and its northeast extent, NDVI and NDWI was incorporated. However, using these two it was still very difficult to identify the extent and the edges of the tail end. Shadows and water in NDWI were difficult to distinguish. Therefore, both were discarded and not unitized whilst digitizing the RTS boundary.

### 3.3.2 RTS directional growth

Based on the digitized RTS polygon it was possible to infer the area of the RTS for each year. This was used to infer change from 1991, 1999 to 2025, which made it possible to calculate mean annual retreat and total growth of the RTS. All calculations were performed in Microsoft Excel.

To better understand the RTSs directional growth, lines were drawn along which the RTS's expansion was measured. These lines extended from a geometric center of the 1991 RTS. From that point (X: 490410.5323000001m, Y: 7496174.2656m, WGS 1984 UTM Zone 53N) azimuth lines extended, from 0° (north) to 340°, in 20° increments. Then the growth along each particular line was calculated in Microsoft Excel after each line was clipped to the RTS's boundary of the particular year and the lines length of was subtracted from the previous year, to receive annual growth. Additionally, the mean growth was calculated by averaging growth along each line in one year.

This method not only shows the directional growth but shows how much the RTS has grown each year in a certain direction. This makes it more accurate to estimate the actual growth of the RTS each year, compared to percentages or annual total growth or total rate of change. It also doesn't show interannual noise which would be shown when comparing each year change to climate data. The years 2000 and 2001 were omitted for this analysis due to insufficient satellite image quality, and therefore potential error source.

### 3.3.3 Slope

Topographic analysis was performed in ArcGIS Pro, in order to understand slope variability around the RTS and within the RTS itself for detection of depressions and stream beds. A Slope and hill shade layer was created using ArcticDEM 2m which was projected into the correct coordinate system (WGS 1984 UTM Zone 53N).

### 3.3.4 Climate analysis

Climate analysis was conducted, using Microsoft Excel. Monthly mean air temperature and total monthly precipitation were analyzed over the study period to identify climatic trends and variability. Seasonal analyses focused on summer (June, July, August), autumn (September, October, November), winter (December, January, February), and spring (March, April, May) conditions, with winter including December from the preceding year. Summer temperatures were examined in particular, as this is the period during which daily temperatures are predominantly above 0 °C. Thawing Degree Days (TDD) were defined as days with mean air temperatures above 0 °C. The annual number of days exceeding this threshold was calculated to evaluate potential changes in the length of the thaw season over time. These data were used to assess whether seasonal temperature shifts, including warmer summers and later onset of winter conditions, have occurred throughout the study period.

### 3.3.5 Climate vs RTS- statistical analysis

A regression analysis was performed in Microsoft Excel to examine the relationship between yearly mean expansion along 20 transect lines and climate variables, including mean annual temp, seasonal mean temp, annual precipitation, seasonal sum of precipitation, thawing degree days (TDD). This analysis was carried out to determine whether any statistically significant relationships exist between these climate variables and RTS change over the period 1999-2025. Due to poor image quality, observations from 2000 and 2001 were excluded from the analysis, as they might have introduced errors.

Additionally, a Mannn-Kendall test was performed to statistically assess whether the variables show a monotonic upward or downward trend over time. The test was performed in Anaconda (Version 3.12.0) using a Python script. The script and its resulting graphs were created with the help of an AI tool (Claude Code).

# 4 Results

## 4.1 Analysis RTS growth

The Batagay thaw slump has progressively increased in size over the study period (1991,1999-2025) (see *Figure 5*). In 1991 the RTS appears relatively narrow, though by 1999 it has already

noticeably expanded. Subsequently, continuous expansion is evident thereafter, with areal growth visible across each successive year. The most pronounced growth occurs in the south western direction, where the RTS takes on a rounded shape. The narrow tail end of the RTS, extending in northeastern direction widened slightly and elongated further north. With further expansion following 1999 the thaw slump developed a more pronounced, tadpole-like shape. While the head of the RTS expanded noticeably, the elongated northeastern tail retained a uniform shape. However, a northwestern extension is observable between 2015 and 2016. A slight rift becomes visible in 2020 and grows increasingly prominent in the following years, remaining distinct and continuing to widen as the RTS expands further from 2024 to 2025.

This spatial expansion can be seen and is further reflected in the quantitative area measurements (see *Figure 6*). The RTS shows a consistent increase in area throughout the study period, following an almost linear growth pattern. As illustrated in figure 3, continuous expansion pattern can be observed with no evident periods of stagnation or acceleration. The mean annual growth rate over the 1991-2025 period was 27367 m². At the start of the observation period in 1991 the thaw slump extended over an area of 135,601 m², growing to an area of 256,151 m² by 1999. For this interval there is no annual in-between observation available. The total area of the thaw slump has expanded to a total area of 874,558 m² by 2025, of which 618,407 m² increase occurred after 1999. By 2025, the latest observation period, the thaw slump has a diameter of 1,037m, from the northeast to the southwest, and a length of 2,468 m, from the southeast to the northwest.

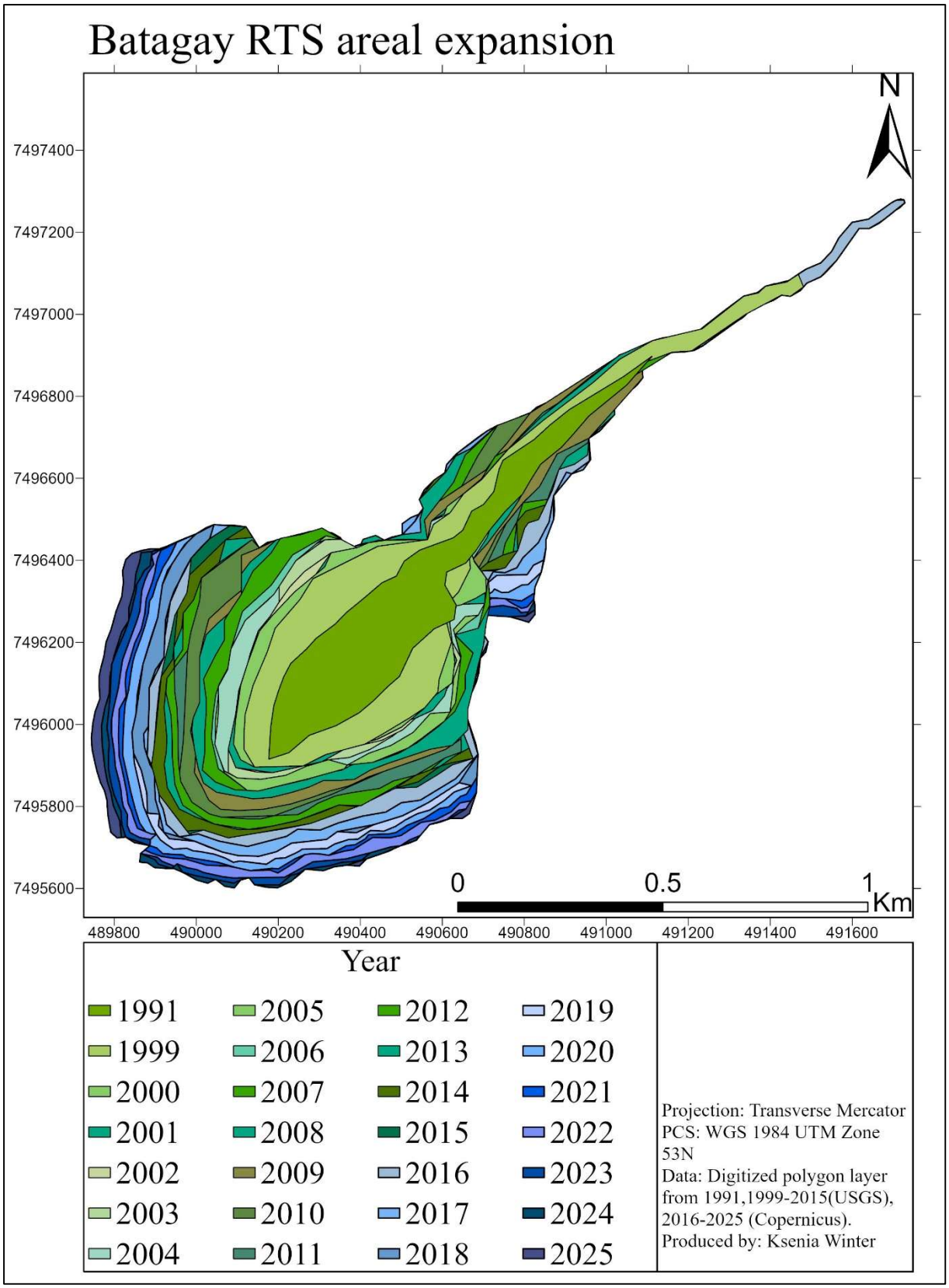


*Figure 5. Batagay RTS area for the years 1991,1999- 2025 digitized based on satellite imagery Landsat 8, USGS (1991, 1999-2015) and Sentinel-2, Copernicus (2016-2025).*

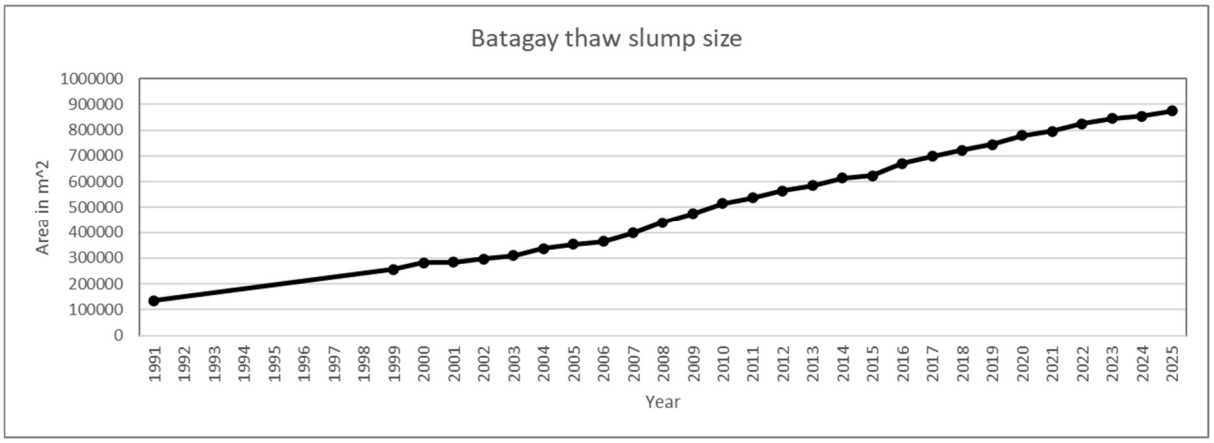


*Figure 6. Annual area (in m²) of Batagay RTS for 1991, 1999-2025 derived from manually digitized polygons of satellite imagery (see Figure 5).*

Annual RTS growth rates show considerable interannual variability, with expansion rates ranging from 0.9% (2000-2001) to 10.3% (2007-2008) of the preceding years area (see *Figure 7*). The yearly growth alternates between periods of rapid expansion and relative stability, reflecting large fluctuations in the rate of change over time. An initial growth rate of 10.2% is recorded for the 1999-2000 interval, followed by comparatively smaller areal changes in successive years. The most active period of thaw slump yearly expansion occurs between 2006 and 2010. During this period growth rates are notably high relative to prior and subsequent years, peaking at 10.3% (2007-2008). Following this expansion peak, relative expansion rates decrease progressively. From 2021 onward, annual growth rates generally decrease. While the RTS continues to expand yearly, thereby adding substantial amounts of absolute area, the percentage-based growth rates indicate that the year-to-year expansion has not accelerated in recent years. Instead, rather a trend towards stabilization is apparent, as more recent intervals shows a comparatively moderate growth. Noticeable here is that in periods such as 2016-2017 (4.1%),2019-2020 (4.6%) and 2021-2022 (3.6%) and 2022-2023, the absolute area added remains substantial, while the percentual increase is comparatively small. Thus, as the RTS grows larger over time, even relatively small increases in percentages appear as large absolute area gain.

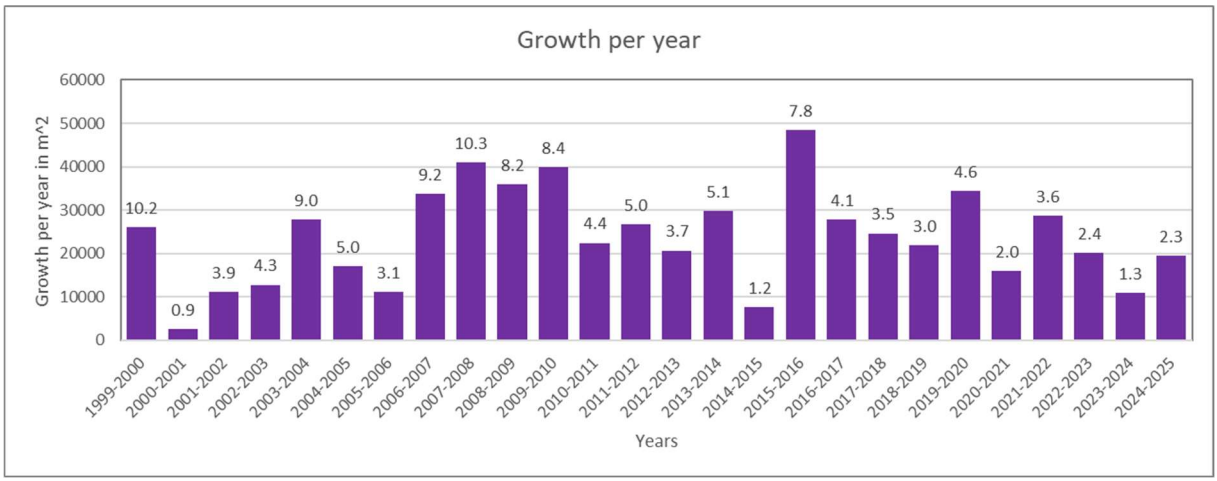


*Figure 7. Yearly absolute area change (m²) and relative change (%), 1999 - 2025 derived from manually digitized polygons of satellite imagery (see Figure 5).*

## 4.2 Directional Growth

Spatial analysis over the 1999-2025 period reveals a clear asymmetry of the Batagay thaw slumps expansion direction. As observed previously in figure 2, expansion does not occur uniformly in all directions. The growth is predominantly concentrated in the southwestern head region, while the northeastern tail remains largely stable and unchanged. This strong asymmetrical expansion is highlighted by the analysis of radial expansion along transects of 20° increments (see *Figure 8, Table 1*). The greatest expansion can be observed along the 240°, 260°, 280° transects. Here the RTS grew by 387m, 394m and 385m respectively. A zone of moderate directional expansion lies between 140° and 180°, while overall growth between 0° and 120° is minimal. Here smallest changes are recorded along the 0° transect, with 34m, and the 40° transect, with 49m. The overall dimension of the RTS can be inferred by measuring along multiple cross-sectional axes. Here the diameter along the 300°-120° axis measures 818m, while the 240°-60° axis measures 1,233m and 220°- 40° axis reaches 1522m.

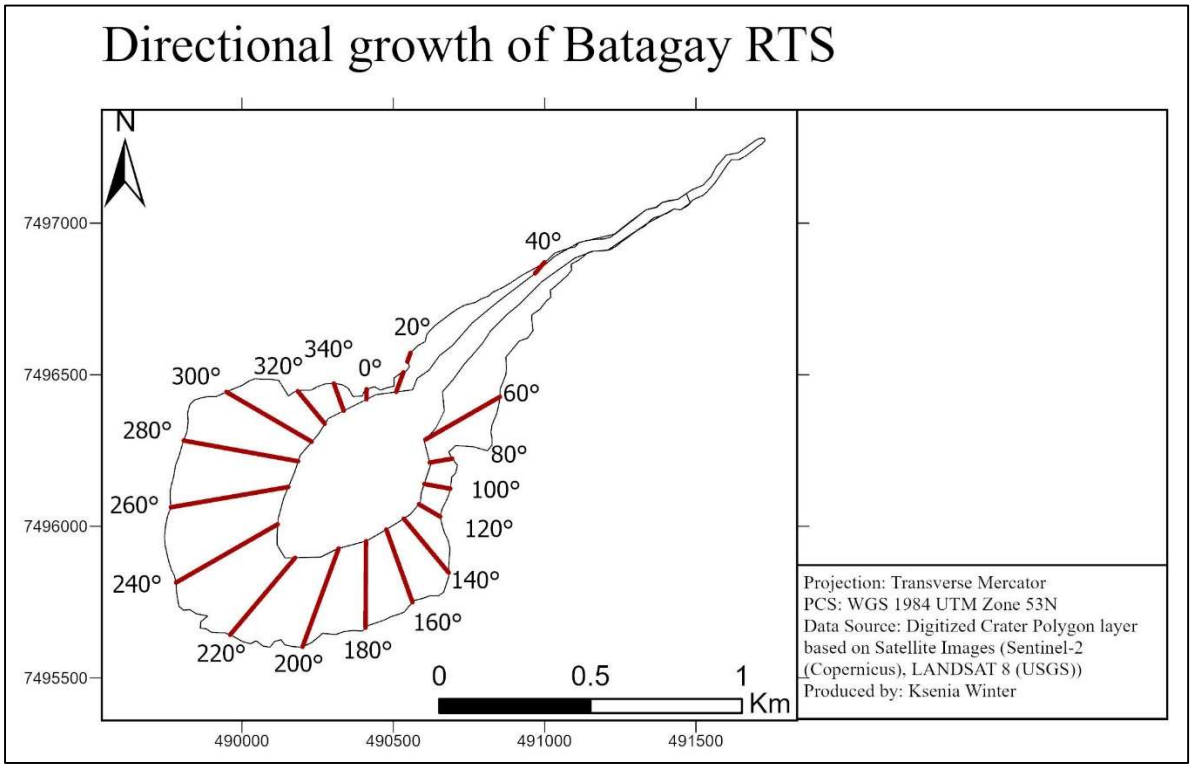


*Figure 8. Directional growth of RTS, 1999 to 2025, along radial transects spaced at 20° intervals (red lines).*

*Table 1. Radial transect growth measurements between 1999 and 2025 of the Batagay RTS, showing change in meters along 18 radial transects at 20° intervals.*

| Angle in Degrees | Change in m | Angle in Degrees | Change in m |
|---|---|---|---|
| **0** | 33.82 | **180** | 285.54 |
| **20** | 100.59 | **200** | 346.11 |
| **40** | 49.17 | **220** | 333.21 |
| **60** | 284.49 | **240** | 387.23 |
| **80** | 75.84 | **260** | 394.02 |
| **100** | 87.91 | **280** | 384.81 |
| **120** | 81.8 | **300** | 326.74 |
| **140** | 232.43 | **320** | 140.25 |
| **160** | 255.47 | **340** | 96.43 |

Analyzing the mean annual growth across all transect lines reveals stark interannual variability (see *Figure 9*). The thaw slump expands by different amounts from year to year, with no notable temporal pattern. The smallest mean annual expansion can be observed in 2024, 2m, and the largest in 2008 where the RTS expanded by a mean of 18m across the transects. Particularly high expansions occurred in the years 2004, 2007, 2008, with additionally high values registered in 2010, 2016,2017 and 2020.

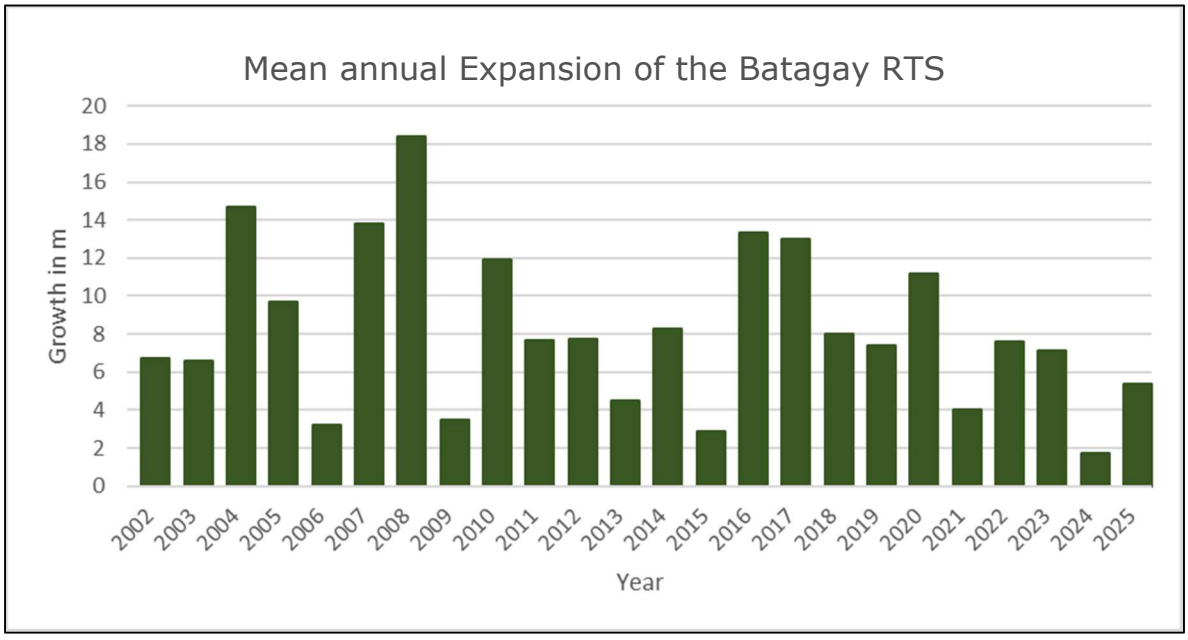


*Figure 9. Mean annual RTS retreat (2002-2025) averaged across all 18 transect lines.*

## 4.3 Slope conditions

The Batagay RTS is situated on the northeastern slope of a hill, positioned just south of a topographic low that lies between two hills (see *Figure 10*). The slope, on which the RTS lies appears to have a gentle slope, while the hill to the northeast of the RTS has a rapid change in elevation. A gully from the northeast to the southwest runs through the RTS. North of the RTS a slight depression can be seen, which appears shallower than the RTS. The thaw slump itself forms a distinct depression, with a greater depth compared to its surrounding terrain. Internally, the RTS shows a great relief variation, reflected by its slope angles and gradients (see *Figure 11*). Visible stream beds and zones of great slope variability show that the RTS floor is not a flat, uniform surface. Additionally, the RTS shows a great topographic contrast with steep slopes dominating the southwestern area, whereas gradually shallower terrain prevails closer to the northeastern RTS boundary.

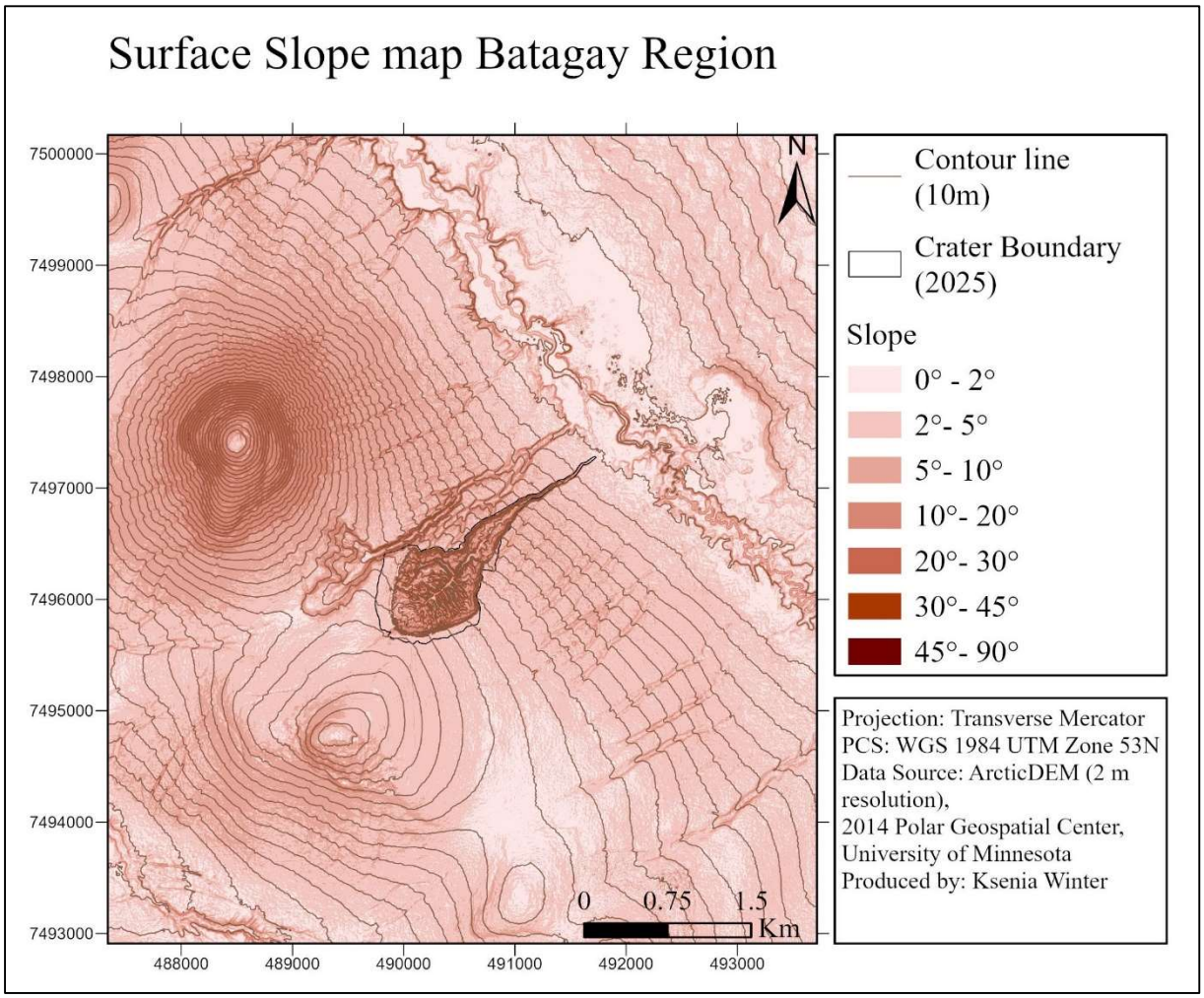


*Figure 10. Surface Slope with 10m elevation contours derived from ArcticDEM 2m.*

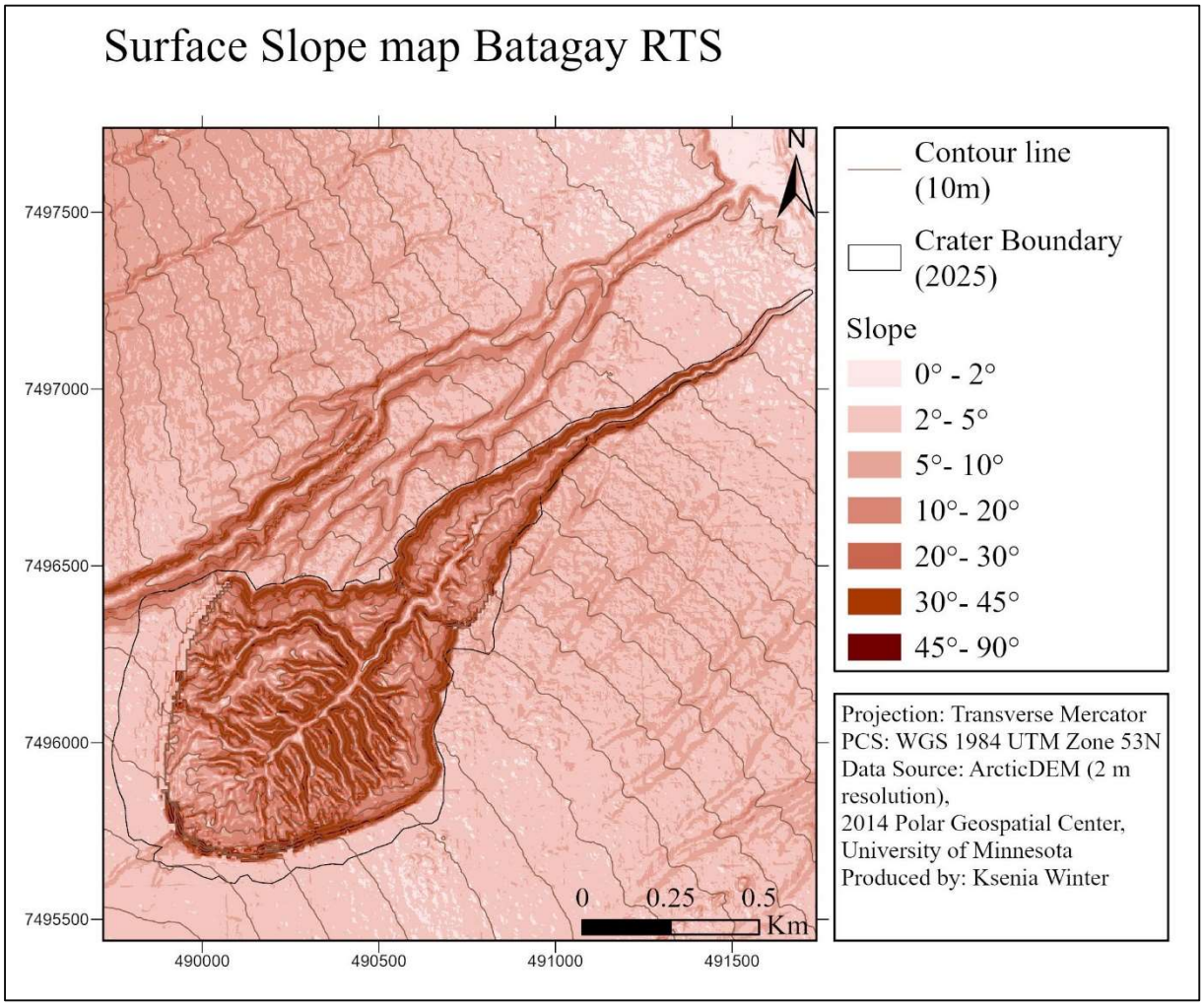


*Figure 11. Surface Slope of Batagay RTS with 10m elevation contours derived from ArcticDEM 2m.*

## 4.4 Climate

Whilst comparing three temperature graphs, retrieved by different methods and areas it becomes clear that there are variations in reported mean annual temperature (see *Figure 12*). Both ERA5-Land temperature curves show very similar temperatures over the Batagay RTS and the city Verhonyansk. The meteorological station, situated in Verkhoyansk, measures overall colder mean annual temperatures, with a mean temperature (1982-2025) being -13.89°C, which is -1.69°C lower than Verkhoyansk ERA5-Land temperatures and -1.49°C than ERA5-Land Batagay RTS. The weather station mean annual temperature shows great spikes from 1982 to 2010, which are not present in the ERA5-Land data. After 2010 temperature ranges decrease in their magnitude and differences between the different data sources. After 2002 the weather station data follows the same trend as the ERA5-Land temperatures but with lower temperatures. With weather station measurements showing particularly low annual mean temperatures in 1992, 2001 and 2004 compared to the satellite inferred data. In the years 1987 and 1996 weather station showcases warmer temperatures.

Comparing the annual precipitation from Era 5land and Verkhoyansk meteorological station the meteorological station underscores in every year (see *Figure 13*). Annual precipitation maximum by, 276mm in 2016, in the same year but 432.9mm era 5.

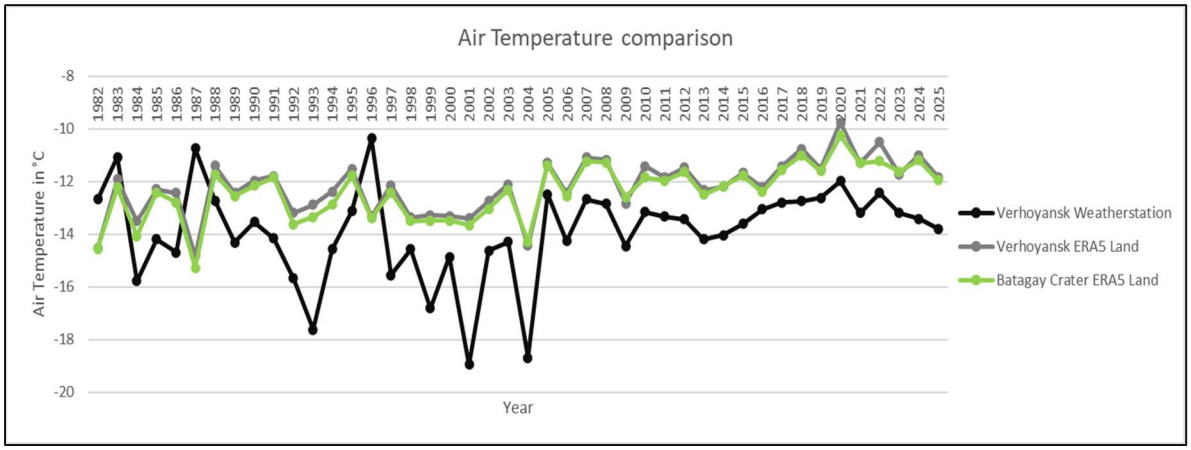


*Figure 12. Mean annual air temperature (in C°) over the time period 1982-2025 collected by Verkhoyansk meteorological station (illustrated in grey), Satellite data averaged over Verkhoyansk (illustrated in black) and Batagay RTS (illustrated in green).*

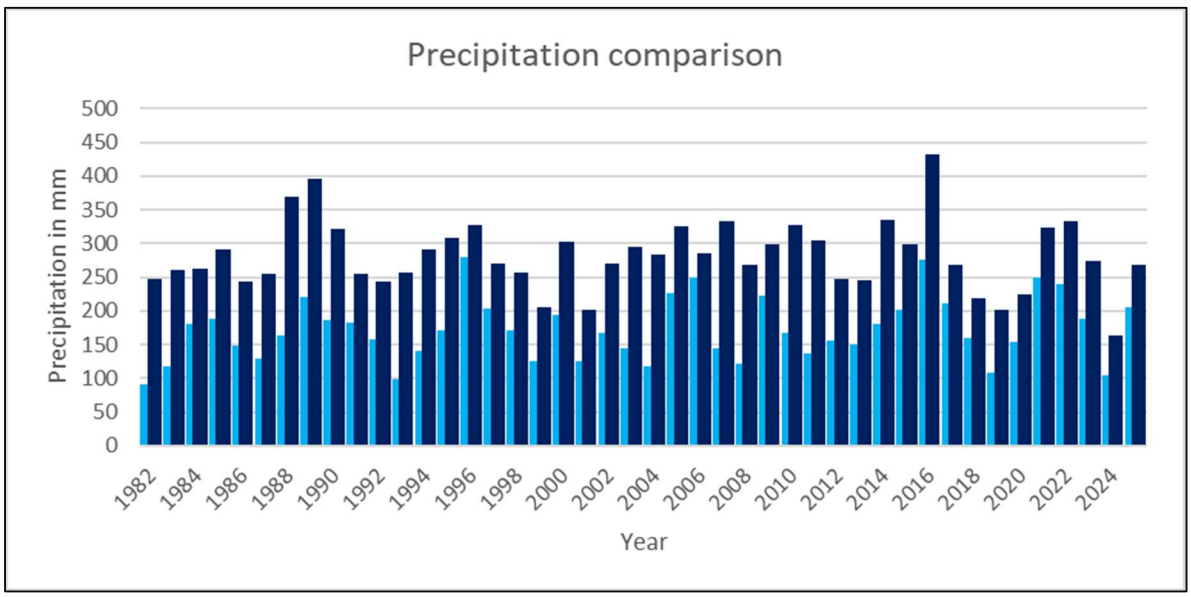


*Figure 13. Annual precipitation collected by ERA5-Land (dark blue) over Batagay RTS, and from Verkhoyansk meteorological station (light blue).*

Looking at the seasonal trends over the Batagay RTS it is interesting to see different patterns (see *Figure 14*). Winter temperatures, having an average of -39°C, are getting lower over the time period, which can be seen due to the negative trendline (*Figure 14*). The temperatures over the 44 years are ranging between -41°Cand -35°C. An especially cold year was 2001, while 1981 and 2025 represent the warmest winter records. Spring temperatures, in contrast, are rising although with some fluctuations ranging from -12°C to -7°C, with 1989 having a particularly warm spring. The summer mean temperature lies at 13.5°C, ranging from a minimum seasonal temperature of 10°C to a maximum of 16.6 °C. This season showcases the steepest warming trend of all seasons, due to increasing temperatures. 2017 had a particularly warm spring followed by an unusually cold summer. The mean seasonal temperatures in autumn are ranging from -11°C to -16.1°C. Notably, 2025 shows colder summer and autumn temperatures again,

contrasting the general warming trend. The long summer period (May-September), *Figure 15*, shows a general temperature increase.

Annual mean temperatures show a clear and consistent rise from 1981 to 2025. Standing out as particularly warm years are 2007 and 2008 (see *Figure 16*). Overall, mean monthly temperatures indicate an intensification of temperature extremes with warmest mean monthly temperatures getting warmer, whilst colder temperatures are further decreasing (see *Figure 17*). There is a large difference between the coldest and warmest temperatures (52.85°C) (see *Figure 17*). The minimum temperature stays consistent over the period of 1981 to 2025, as the trendline is horizontal. This indicates that the temperature is relatively stable, however the minimum temperatures are dropping slightly lower over time. In contrast the maximum temperature is increasing, notable from the upward trendline, therefore the temperature difference between mean monthly minima and maxima is growing.

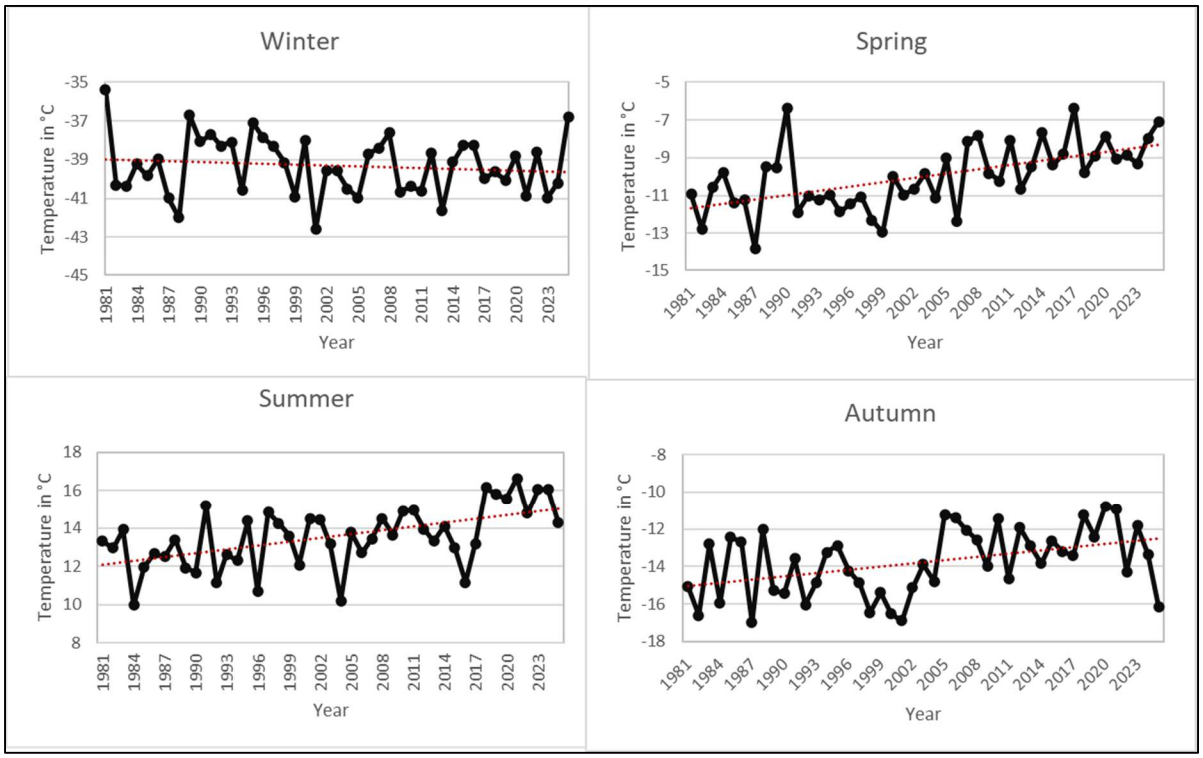


*Figure 14. Mean seasonal temperature in °C from 1981 to 2025. Winter (Dec,Jan,Feb), Spring (Mar,Apr,May), Summer (Jun,Jul,Aug), Autumn (Oct,Nov,Dec).*

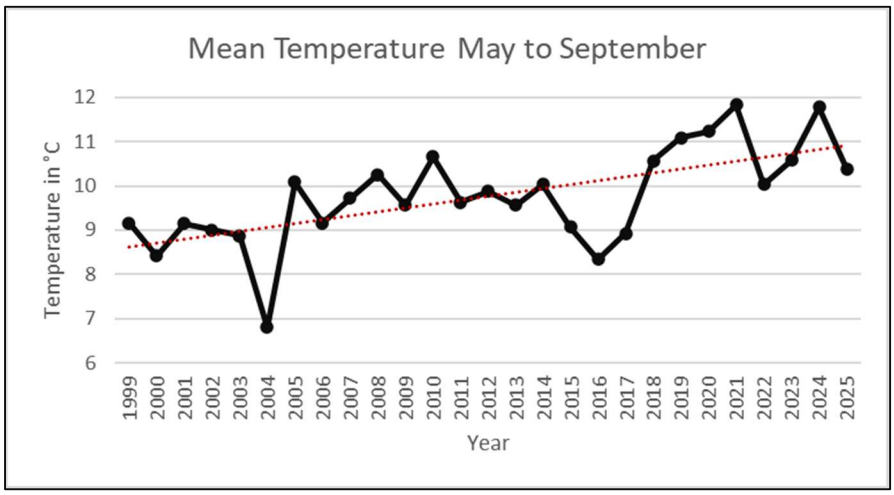


*Figure 15. Mean annual temperature for May-Sep in °C from 1981 to 2025.*

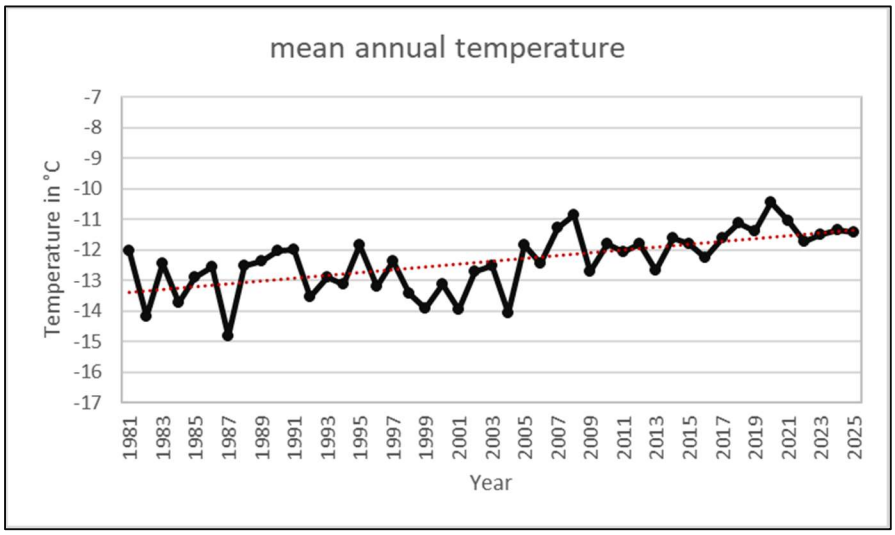


*Figure 16. Mean annual temperature in °C from 1981 to 2025.*

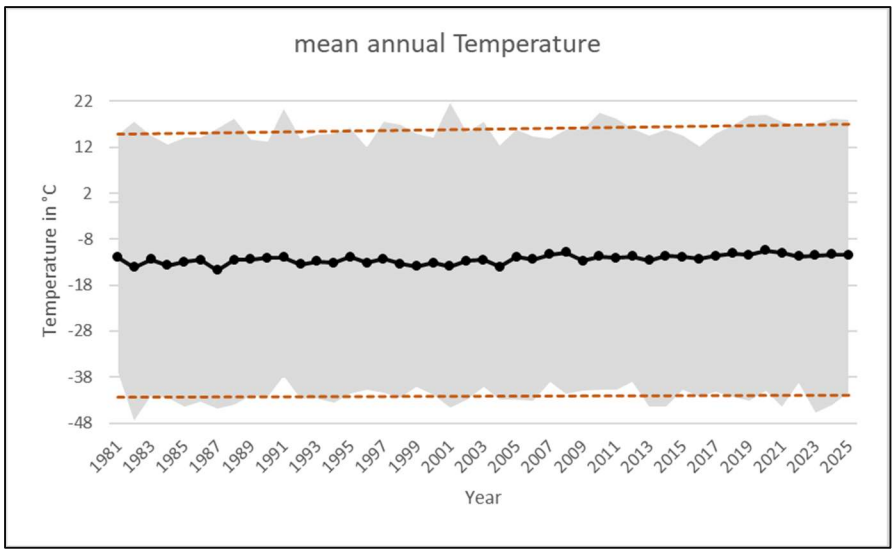


*Figure 17. Mean annual temperature taken from ERA5-Land over the years 1981 to 2025 and the minimum and maximum monthly temperature of the year.*

Looking at Days above 0°C, thawing degree days (TDD) and days below 0°C, freezing degree days (FDD) side by side, there is an increase in TDD and a decrease in FDD (see *Figure 18*). A seasonal shift is not detected with earlier spring onset or later autumn freeze as the trend line is horizontal (see *Figure 19*).

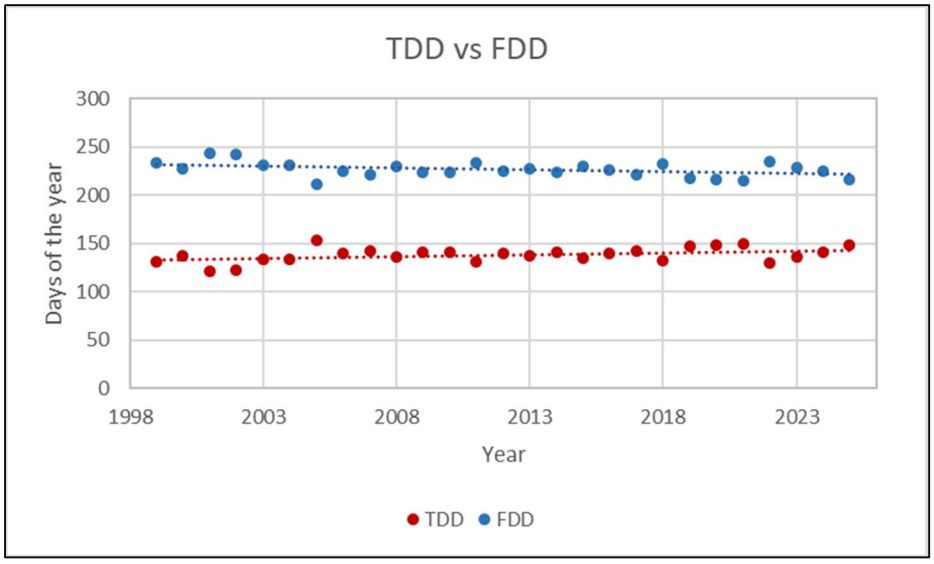


*Figure 18. TDD and FDD in days of the year from 1999 to 2025.*

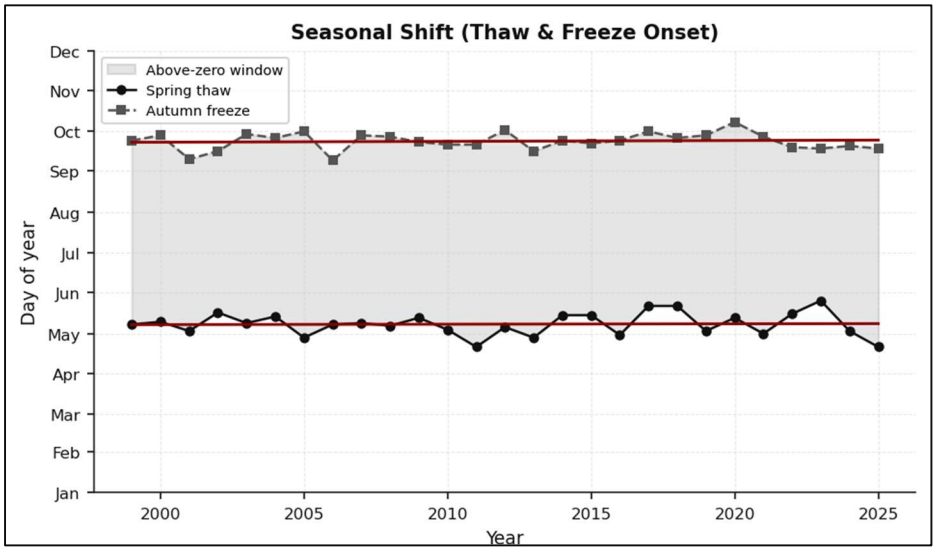


*Figure 19. Seasonal shift in days of the year from 1999 to 2025.*

Overall, the area in which the Batagay RTS is situated is very dry with a maximum annual precipitation of 432mm (see *Figure 20*). Precipitation remains stable between 1981 and 2025, although certain years (1988, 1989, 2016) receive above average precipitation. The period from 2002 to 2011 received larger amounts of precipitation before declining again. 2024 is a year which was exceptionally dry with a recording of 163mm.

A clear seasonal pattern arises, with the months May to September receiving highest amount of precipitation throughout the year (see *Figure 21*). Mean precipitation peaks in July with

51.42mm, whereas February is the driest month with 4.12mm on average. Despite this noticeable seasonal variability, the climate remains dry.

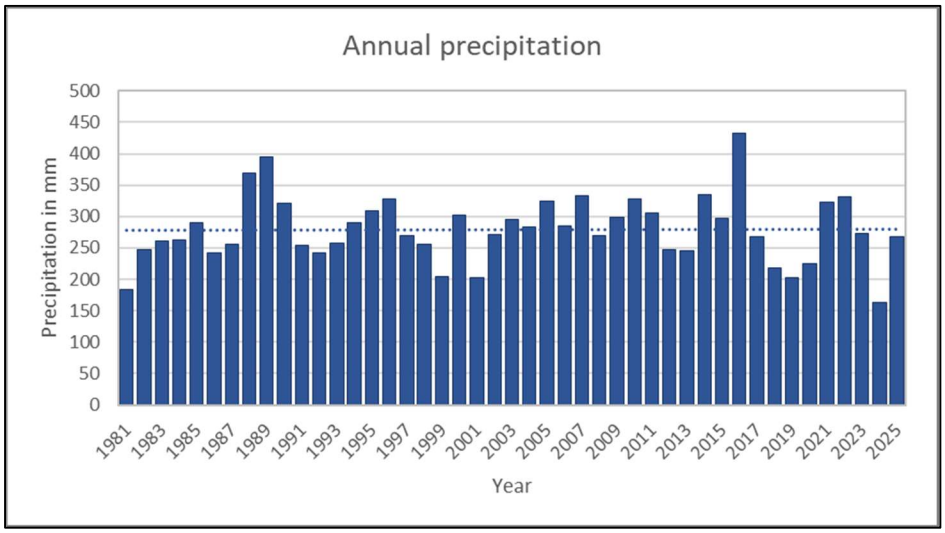


*Figure 20. Sum of annual precipitation in mm from 1981 to 2025.*

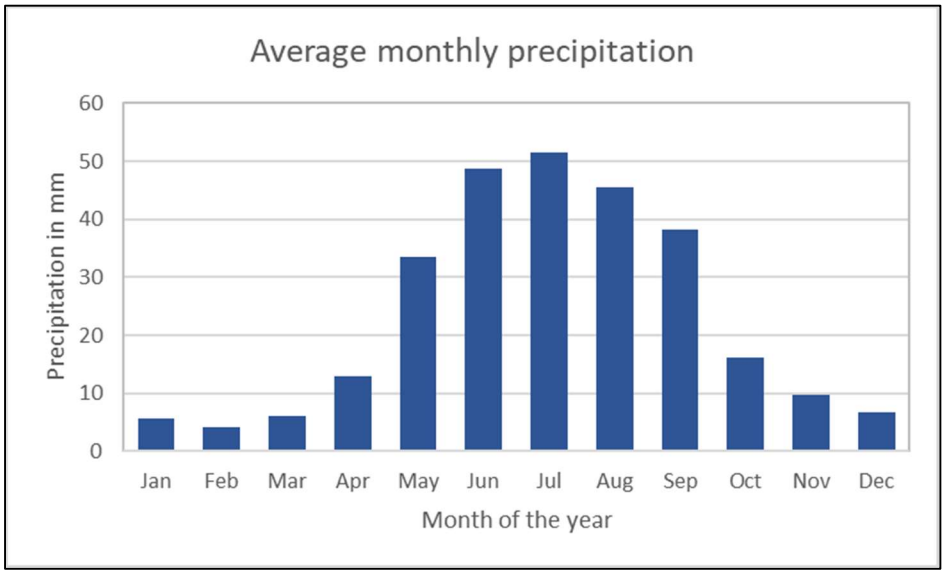


*Figure 21. Mean monthly precipitation in mm from 1981 to 2025.*

## 4.5 Analysis Climate and RTS growth

Annual mean RTS growth along all the 20° transect lines is compared to both climate variables of the same year and the preceding year. A lagged comparison is included, as geomorphological and permafrost processes are not always instantaneous. They often respond to climatic conditions with a delay in time. For example, the thawing of permafrost due to elevated temperatures might not occurs immediately within the same year, but due to cumulative thermal influence of the previous year. Warmer temperatures may deepen the active layer gradually or accelerate the degradation of the ice complex which leads to RTS expansion. Precipitation is also relevant, as snow fall in a year can act as an insulator, reducing winter cooling. Rainfall during the warmer months, in contrast, can accelerate degradation processes. These effects might not be immediate and therefore a lagged response is worth considering. Incorporating

both same and one- year lagged comparison, the analysis captures whether there is a delayed response in thaw slump expansion, providing a more complete understanding of the relationship between climate and growth.

The no-lag regression analyses whether RTS growth is directly linked to the climate variables of the same year. Across all climate variables, none of the relationships are significant, indicated by the p-values, which are all above 0.05 and the low $R^2$ values (see *Table 2*). Looking at temperature, there is no significance for annual temperature and seasonal temperatures. Spring and summer temperatures have a stronger association with RTS growth, seen by their high $R^2$ values (0.062, 0.095), although nor statistically significant. Autumn mean temperatures as well as TDD show no significance with RTS growth. The absence of any significant relationship indicates that growth does not respond immediately to climate conditions. The one-year lag analysis shows a statistically significant relationship between RTS growth and summer temperatures, both from May to September and June to August (see *Table 3*). Summer mean temperature is the strongest indicator, with a p-value of 0.018, whilst long summer, with a p-value of 0.05 and $R^2$ of 0.164 has a weaker significance. The negative slopes indicate that increasing temperatures lead to reduced RTS growth. All other climatic variables are non-significant. Based on the regression analysis performed between RTS mean growth and precipitation for the same and preceding year, no significant relationship between RTS growth and amount of annual or seasonal precipitation was found (see *Table 2,3*).

*Table 2. Results of regression analysis between climate variables of the same year and RTS mean annual growth along all 18 transect lines.*

| No lag | | | | | | |
|---|---|---|---|---|---|---|
| **Predictor** | **SS slope** | **Std Error** | **$R^2$** | **Adjusted $R^2$** | **p-value** | **Significance** |
| Mean annual temp.(°C) | 0.443 | 4.328 | 0.006 | -0.039 | 0.713 | no |
| Winter mean temp.(°C) | 0.786 | 4.230 | 0.051 | 0.008 | 0.289 | no |
| Spring mean temp.(°C) | 4.205 | 4.205 | 0.062 | 0.019 | 0.241 | no |
| Summer mean temp.(°C) | -0.845 | 4.130 | 0.095 | 0.054 | 0.142 | no |
| Autumn mean temp.(°C) | 0.207 | 4.331 | 0.005 | -0.040 | 0.741 | no |
| Long summer (May-Sep) | -1.124 | 4.147 | 0.088 | 0.046 | 0.160 | no |
| TDD | 0.007 | 4.341 | 0.000 | -0.045 | 0.959 | no |
| Annual precipitation (mm) | -0.015 | 4.559 | 0.034 | -0.010 | 0.386 | no |
| Winter precipitation (mm) | 0.242 | 4.247 | 0.043 | 0.000 | 0.331 | no |
| Spring precipitation (mm) | 0.045 | 4.243 | 0.045 | 0.002 | 0.320 | no |
| Summer precipitation (mm) | 0.021 | 4.191 | 0.068 | 0.026 | 0.217 | no |
| Autumn precipitation (mm) | -0.024 | 4.310 | 0.015 | -0.030 | 0.573 | no |

*Table 3. Results of regression analysis between climate variables of the previous year and RTS mean annual growth along all 18 transect lines.*

| 1 year lag | | | | | | |
|---|---|---|---|---|---|---|
| **Predictor** | **SS slope** | **Std Error** | **$R^2$** | **Adjusted $R^2$** | **p-value** | **Significance** |
| Mean annual temp.(°C) | -1.183 | 4.213 | 0.059 | 0.016 | 0.255 | no |
| Winter mean temp.(°C) | 0.806 | 4.222 | 0.054 | 0.011 | 0.273 | no |
| Spring mean temp.(°C) | -0.670 | 4.242 | 0.045 | 0.002 | 0.318 | no |
| Summer mean temp.(°C) | -1.310 | 3.811 | 0.229 | 0.194 | 0.018 | yes |
| Autumn mean temp.(°C) | -0.171 | 4.333 | 0.004 | -0.041 | 0.773 | no |
| Long summer (May-Sep) | -1.529 | 3.971 | 0.164 | 0.126 | 0.050 | yes |
| TDD | -0.013 | 4.340 | 0.001 | -0.045 | 0.910 | no |
| Annual precipitation (mm) | 0.022 | 4.146 | 0.088 | 0.047 | 0.159 | no |
| Winter precipitation (mm) | 0.015 | 4.268 | 0.033 | -0.010 | 0.392 | no |
| Spring precipitation (mm) | -0.010 | 4.337 | 0.002 | -0.043 | 0.828 | no |
| Summer precipitation (mm) | 0.015 | 4.268 | 0.033 | -0.010 | 0.392 | no |
| Autumn precipitation (mm) | 0.077 | 3.991 | 0.155 | 0.116 | 0.057 | no |

The scatter plots show relationships between RTS growth and different monthly mean (*Figure 22*). Therefore spring, summer, autumn and winter. Winter mean temperatures show a positive trend for both same year and preceding year and RTS growth. Spring mean temperatures show a positive relationship with same year RTS growth but a negative trend with the preceding year. Summer temperatures show negative trends with both the same year and preceding year, similarly the long summer period also shows decreasing trends (see *Figure 23*). The near horizontal trendline for autumn in both cases, indicates no relation to RTS growth. Annual mean temperature shows a slight positive trend for the same year but a negative trend when lagged (see *Figure 23*). Precipitation shows a positive trend both the same year and lagged year comparison, suggesting higher precipitation can be increase RTS growth (see *Figure 23*). RTS growth comparison to TDD produces an almost horizontal trendline, indicating that there is no significant relationship.

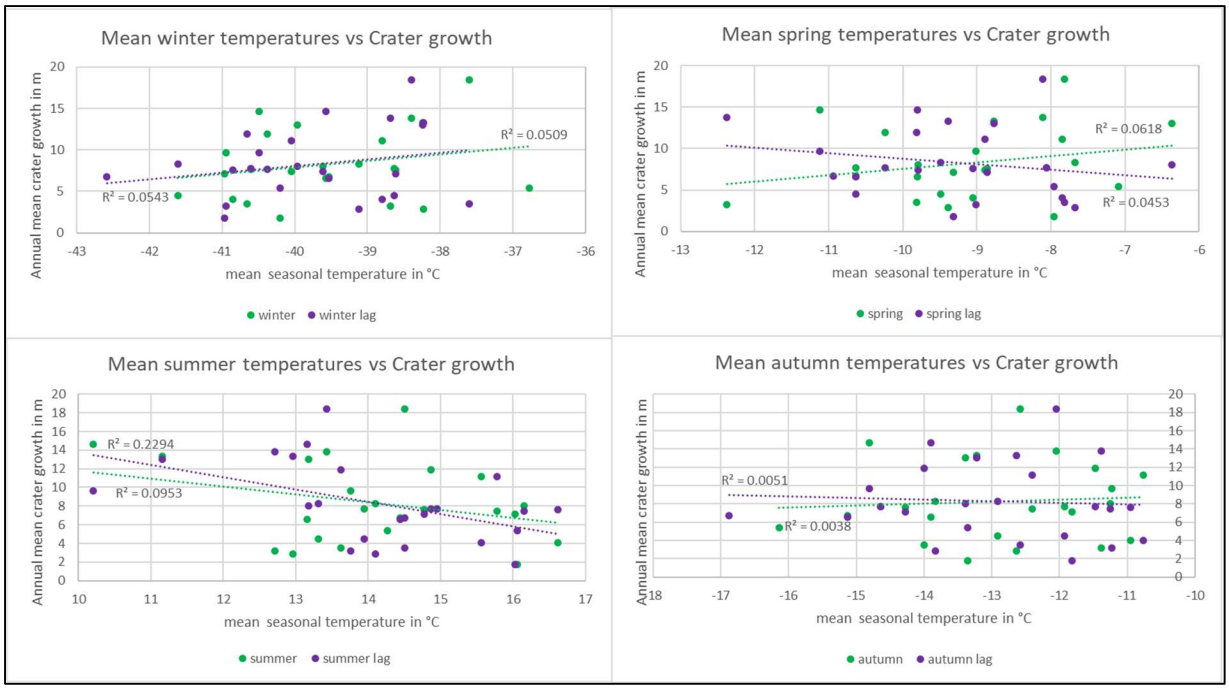


*Figure 22. Mean annual RTS crater growth in m (y axis) against mean seasonal temperatures for Winter (Dec-Feb), Spring (Mar-May), Summer (Jun-Jul), Autumn (Sep-Nov), derived from ERA5-Land, (x axis) for the period 2002-2024.*


*Figure 23. Mean annual RTS crater growth in m (y axis) against climatic variables, precipitation, TDD, annual mean temperature and long summer (May-Sep) (derived from ERA5-Land, (x axis) for the period 2002-2024.*

The relationship between RTS growth and timing of spring thaw and autumn freeze onset day of the year show no significant relationship between the onset timing (see *Figure 24*). This is true for the same year and lagged response. Although regression slopes were slightly positive, the low $r^2$ values of spring same year and lagged, autumn same year and lagged (0.00, 0.03, 0.02, 0.03) indicate that seasonal thaw and freeze timing do not explain the interannual variability in RTS growth rates.

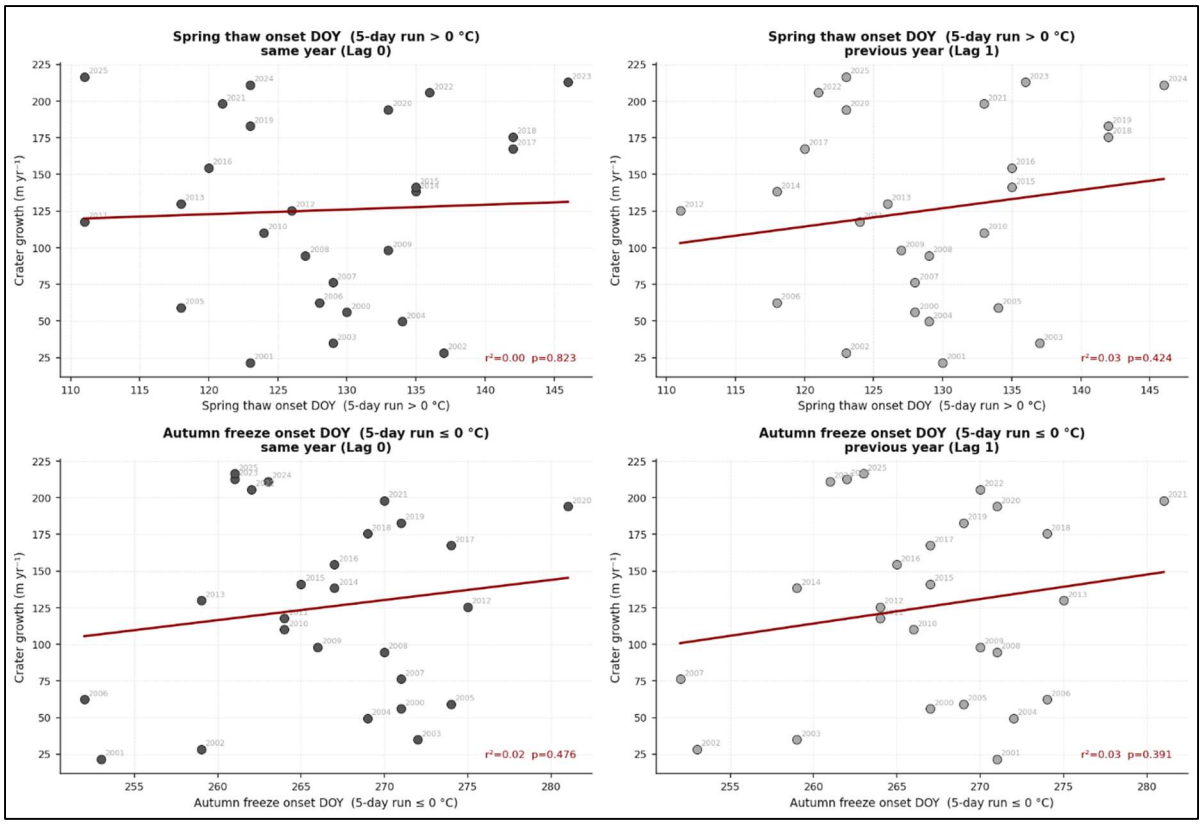


*Figure 24. Spring thaw and Autumn freeze onset compared to RTS growth in m along lines. For same year 5 days temperature above or below 0°C and previous year.*

The Mann-Kendall test results indicate overall warming trend across most temperature series, with warming being most pronounced during spring and extended summer periods (see *Table 4*). Mean annual temperatures show strong and significant upward trend ($\tau$ =0.54). Spring and long summer temperatures have experienced stark consistent warming trends seen by their low p-values and $\tau$ (p= 0.001, $\tau$ =0.46 and $\tau$ = 0.44, p = 0.001). Summer also shows a significant positive trend. Autumn temperatures show less consistent warming trends, while winter temperatures have no significant trend.

*Table 4. τ, Sen Slope and p-value a Mann- Kendall test results between mean RTS length per lines 2000-2025 and same year climate temperatures.*

| **Same year** | **τ** | **Sen Slope** | **p-value** |
|---|---|---|---|
| **Mean annual temperature** | 0.54 | 0.0819 | 0.000 |
| **Winter temperature** | 0.08 | 0.02949 | 0.559 |
| **Spring temperature** | 0.46 | 0.1153 | 0.001 |
| **Summer temperature** | 0.36 | 0.0938 | 0.009 |
| **Autumn temperature** | 0.25 | 0.0987 | 0.073 |
| **Long summer temperature** | 0.44 | 0.0855 | 0.001 |

# 5 Discussion

The results of this study showed that RTS growth can be monitored by the digitization of satellite images (see *Figure 5*). The digitization of the thaw slump was previously done by Vadakkedath et. al., 2020 and Kizyakov et. al., 2024, until the year 2018 and 2023 respectively, although not yearly from 1999 onward, like this study. Vadakkedath et. al recorded slump areas of 19ha in 1991 and 78ha in 2018. The digitized Batagay RTS area in this study presents a smaller area with 0.13ha in 1991 and 75ha in 2018. Whilst Kizyakov et. Al. Presents a RTS size of 87.6 ha in 2023, whereas this study's RTS size is 84.4 ha for the same year. Although the overall size estimation of the RTS differs, with this study's potential underestimation of the total thaw slump area, the growth trajectory is consistent. This method enables the analysis of year-to-year areal growth variability, as illustrated in *Figure 7*, which has not been previously achieved for this site at this temporal resolution.

RTS boundary digitization is influenced by differences in resolution of satellite images, 10m and 30m. The north-eastern extend of the RTS, which becomes shallower and eventually drains into the Batagay river (see *Figure 4, Figure 10)* was particularly difficult to identify due to resolution, resulting in an extend of RTS area towards the northeast from 2015 to 2016. Additionally, boundary identification, due to shadows or poor visibility of edges, may have led to under or over estimation of actual RTS boundary. The majority of Satellite images chosen to be digitized are from August, however some years have scarce data availability, therefore satellite images from other months had to be taken, thereby potentially underscoring growth of RTS that year. A key limitation of this approach is the tracking of solely areal expansion, disregarding volumetric expansion. For this study site a volumetric expansion analysis was not possible as the most detailed DEM layer (ArcticDEM2m) was obtained in 2014. Considering the expansion of the RTS since then, the DEM layer no longer accurately represents the current RTS morphology.

While areal measurements and tracking of the RTSs extend through digitization captures the dimensions of the thaw slumps expansion, it has a limitation. As the RTS increases in size, a minimal or modest relative growth rate will show up as a large absolute increase in area the next year (see *Figure 8*). Therefore, from just the area it is difficult to assess whether the expansion is accelerating, decreasing or stabilizing over time.

In this study the 18 transect line analysis addresses this limitation by providing mean growth in m, of the RTS. This approach captures the mean directional growth for the 20° increments, thereby identifying the headwall, where the RTS retreat is the largest. Additionally, it highlights the directional expansion of the thaw slump. The directional expansion, assessed through this method, identifies asymmetry patterns and headwall retreat, but is limited in accurate

representation of directional growth as 20-degree increments leave large gaps between them, in which cannot be tracked.

As the transect analysis demonstrates (*Figure 9, Table 1*) the expansion of the Batagay RTS is not uniform in all directions. This asymmetrical growth is most likely due to a variety of factors and their complex interplay.

The Batagay RTS is aligned southwest to northeast along a northeastern facing hillslope (see *Figure* 10). As the RTS growths upslope, illustrated in *Figure 10*, the growth in southeastern and northwestern direction might be limited by the reduction and exhaustion of Yedoma as the slump approaches bedrock (Tumskoy et al., 2021; Kizyakov et al., 2022). Furthermore, the alignment leads to the western wall receiving the highest amount of seasonal and annual incoming solar radiation, which likely results in its similar retreat rate (Kizyakov et al., 2022). The southern and southwestern walls, however, are shaded during the midday (see appendix *Figure A5*), which results in slower retreat rates (Kizyakov et al., 2022). Some studies suggest that retreat rates are higher for RTS with southern aspects, whilst others did not make that connection (Lewkowicz, 1987; Lacelle et al., 2015; Wang et al., 2009; Nesterova et al., 2021). The Batagay RTS disproves this connection.

The exceptional size of the RTS with an area of 874,558 m² by 2025, is likely due to Yedoma, debris transport and steep slope gradient (Lacelle et al., 2015, Murton et. al., 2023). These factors prevent the Batagay RTS from stabilizing, as rapid transport of debris into the Batagay river, beyond the thaw slump, ensures the exposure of massive ground ice to warm air temperature and solar radiation. As the slump is located on a hill (see *Figure 10),* the slope provides a transport gradient which allows for fallen or accumulated debris to move away from the ice rich headwall (Kokelj et al., 2015; Kizyakov et al., 2022). Furthermore, debris, through meltwater and rain transport, is facilitated by erosion ravines, which can be seen in *Figure 11*. Additionally, Yedoma and its high ice content results in smaller amounts of debris (Kizyakov et al., 2013; Kizyakov et al., 2022). The sandy soils found in the Batagay RTS allow for easy drainage leading to facilitated thermal erosion (Murton et. al., 2023).

Comparing areal RTS data and mean yearly expansion in meters, their year-to-year pattern of expansion are broadly similar. Both show the years 2003-2004, 2006-2010 as dominant growth intervals. A further phase of expansion lies between 2019 and 2020, although less pronounced. A strength of the transect line measurement method does not incorporate the resolution-based error of increased areal expansion between 2015 and 2016, which appears in *Figure 7*.

Looking at the Batagay RTS growth patterns themselves, the accelerated period of growth between 2004 and 2010 can be linked to climate with the rise in mean annual air temperatures

and increased summer rainfall (Kunitsky et. al., 2013). According to Vadakkedath et.al. (2020) the thaw layer depth was deeper between 2004 and 2010, compared to following years. Additionally, the yearly retreat of the RTS exposes more Yedoma, which in turn thaws and leads to further retreat (Murton, 2023). It is possible that growth slowed down after 2010 due to vegetation succession. This is most intense in central and northern parts where permafrost has already melted and there inhibiting further processes of permafrost melt through their insulating properties (Vadakkedath et.al., 2020). Furthermore, the reduced rate in growth might be due to terrain limitations and geological constrains such as hillslope topography, reduction of ice rich sediments (Kizyakov et. al., 2022).

Although, as previously described in the background, the Batagay RTS growth was initially triggered by anthropogenic activity, studies (Kizyakov et.al., 2024) suggest that the growth is linked to a change in climate. Research highlights that higher temperatures and amounts of precipitation lead to more occurrence and larger size of thaw slumps (Kunitsky et.al., 2013). Therefore, it was interesting to look at regional climate and at its relationship to the Batagay RTS expansion.

The region of the Batagay RTS is warming, which is documented through both meteorological station records and satellite derived temperature data. While satellite data provides consistent spatial and temporal measurements it represents averaged values, thus potentially failing to capture localized anomalies. The Verkhoyansk weather station was initially considered as the primary climate data source. Before instrument changes in 2010 the temperature records showed large temperature fluctuations compared to satellite derived records, and was therefore disregarded for a long-term climate analysis. The satellite climate data may have smoothed temperature extremes that the meteorological station might have captured. The precipitation data used in this study shows monthly and yearly precipitation, therefore intense rainfall events such as storms are missed. These events influence crate growth. Given the study areas low precipitation records, this overlooked rainfall events would likely not have changed the findings of the study.

Seasonal analysis revealed winter cooling and spring, summer and autumn warming. Additionally, a rising amount in thawing degree days extends the period in which the active layer deepens and Yedoma can thaw. Similarly, the observed seasonal shift could facilitate thermal denudation through a longer period of warm temperatures. Kuninsky (2013) links temperature increase to RTS growth. The patterns of RTS growth and temperature are consistent with this indicated relationship, driving thermal denudation, Yedoma thaw and thus RTS expansion.

The statistical regression analysis between year-to-year mean transect line RTS expansion, however, are therefore rather unexpected and differ from previous studies. Here for all tested climatic variables only lagged summer and long summer temperatures were deemed significant. The regression slope is negative, indicating that warmer temperatures are linked to reduced RTS expansion patterns. This is contradicting to existing literature (Kuninsky et. al., 2013; Vadakkedath et. al., 2020; Murton et. al., 2023). Nevertheless, a lagged relationship between temperatures and RTS growth is possible as the ground does not immediately respond to changes in air temperature, but rather the active layer potentially deepens with each consecutive warm summer (Woo, 2012).

These contradicting results might be explained by methodological factors. The sample size of 25 years is relatively small, which limits statistical accuracy, with negative $R^2$, possible by larger residuals than sum of squares, values indicate that there is a possibility that linear regression is not a good model in this case, as the relationship might be nonlinear. Additionally, the RTS retreat measurements along only 18 lines may not capture full picture of year-to-year change. Denser radial lines might have reduced this error.

The Batagay thaw slump might be approaching its maximum limits and therefore decoupling from climatic factors. Overall, the mechanisms driving thermal denudation and RTS retreat are more complex than simple climate and RTS growth relationship, which were performed in this study.

Monitoring RTS in a warming climate is important due to their influence on the global carbon emission, local ecosystems and nearby communities (Makopoulou et al., 2024; Nesterova et al., 2024). The satellite-based monitoring approach is particularly valuable in remote and inaccessible sites.

## 5.1 Future Growth

According to Kunitsky et al. (2013) the Batagay RTS was first recognized as thaw slump in 1991, meaning that by 2025 it had experienced its thirty fourth summer. RTS stabilize typically thirty to fifty summers or after the ground ice is exhausted and bedrock reached (French, 2018). Further lateral growth of the RTS is limited by bedrock proximity and exhaustion of ground ice content, while further deepening will mostly be inhibited by underlying bedrock geology (Kizyakov et al., 2024).

# 6 Conclusion

Satellite image-based digitization of the Batagay retrogressive thaw slump boundary over the period 1999-2025 produced extent estimates that are consistent with existing literature, while providing the most complete temporal record of expansion to date. The RTS area has been expanding continuously over time with growth accelerating until 2010, after which periods of

fluctuating growth patterns followed. The Batagay RTS growth is spatially asymmetrical, due to local topography, slope aspect and ground ice distribution. Meltwater drainage prevents sediment accumulation and thus sustaining the headwall exposure. This drainage in combination with high ice content in the soil leads to its exceptionally large size, compared to other RTS.

Climate analysis identified rising trends for annual mean temperature, as well as seasonal temperatures, in particular spring and summer. A regression analysis between the RTS expansion and climatic variables showed no statistical significance overall, except for RTS slower retreat rates in warmer temperatures, when coupled with preceding years summer mean temperatures. However, no statistically significant relationship was detected between retreat rates and temperatures of the same year. Neither same year or preceding year precipitation showed a statistically significant relationship with RTS growth.

Although no significant relationship was found between Batagay RTS growth and climatic variables in this study, broader literature identifies RTS development as a process of permafrost degradation dependent on climate. As permafrost thaws, previously frozen organic carbon is released, thereby affecting the global carbon cycle.

The complex dynamics of the Batagay RTS display broader processes of permafrost degradation and thermokarst development, highlighting potential vulnerability of ice rich permafrost regions under continued climate warming.

# 7 References


Are F. E. (1980), Thermal Abrasion of Seacoasts [in Russian]

Barreto, M. S. C., Wani, R. P., Goranov, A. I., Sowers, T. D., Fischel, M., Douglas, T. A., Hatcher, P. G., & Sparks, D. L. (2024). Carbon Fate, Iron Dissolution, and Molecular Characterization of Dissolved Organic Matter in Thawed Yedoma Permafrost under Varying Redox Conditions. *Environmental Science & Technology*, *58*(9), 4155–4166. https://doi.org/10.1021/acs.est.3c08219

Barry, R. G., & Gan, T. Y. (2022). Frozen ground and permafrost. In *Cambridge University Press eBooks* (pp. 207–238). https://doi.org/10.1017/9781108767262.007

Biskaborn, B. K., Smith, S. L., Noetzli, J., Matthes, H., Vieira, G., Streletskiy, D. A., Schoeneich, P., Romanovsky, V. E., Lewkowicz, A. G., Abramov, A., Allard, M., Boike, J., Cable, W. L., Christiansen, H. H., Delaloye, R., Diekmann, B., Drozdov, D., Etzelmüller, B., Grosse, G., … Lantuit, H. (2019). Permafrost is warming at a global scale. *Nature Communications, 10*, Article 264. https://doi.org/10.1038/s41467-018-08240-4

Boike, J., K. Roth, and P. P. Overduin. 1998. Thermal and hydrologic dynamics of the active layer at a continuous permafrost site (Taymyr Peninsula, Siberia). *Water Resources Research*, 34: 355-363. DOI: 10.1029/97wr03498

Burn, C. R. (2020). Transactions of the International Permafrost Association number 3. *Permafrost and Periglacial Processes*, *31*(3), 343–345. https://doi.org/10.1002/ppp.2058

Burn, C. R. (2020). Transactions of the International Permafrost Association Number 3. Permafrost and

Canadian high Arctic and their response to climate and terrain factors. *Environmental Research Letters*, *14*(5), 055006. https://doi.org/10.1088/1748-9326/ab12fd

Danilov, P. P., Boeskorov, V., Savvinov, G. N., & Schirrmeister, L. (2019). Past climate and continentality inferred from ice wedges at Batagay megaslump in the Northern Hemisphere's most continental region, Yana

Highlands, interior Yakutia. *Climate of the Past*, *15*(4), 1443–1461. https://doi.org/10.5194/cp-15-1443-2019

European Space Agency. (accessed on 26.05.2026). Copernicus Data Space *Sentinel-2 Level-2A multispectral imagery.* https://browser.dataspace.copernicus.eu/

French, H.M. (2018). The periglacial environment. Fourth Edition.

*IPCC (n.d). Changes in the Active Layer - AR4 WGI Chapter 4: Observations: Changes in Snow, Ice and Frozen Ground.* https://archive.ipcc.ch/publications_and_data/ar4/wg1/en/ch4s4-7-3-1.html#:~:text=Increases%20in%20summer%20air%20temperature,increase%20in%20active%20layer%20thickness.

Japan Meteorological Agency (JMA). (accessed 26.05.2026) *ClimatView climate normals — Verkhoyansk station (WMO ID: 24266)*. World Climate / TCC. https://ds.data.jma.go.jp/gmd/tcc/tcc/products/climate/climatview/graph_mkhtml_nrm.php?n=24266&m=1

Jones, M. K. W., Pollard, W. H., & Jones, B. M. (2019). Rapid initialization of retrogressive thaw slumps in the

Kizyakov, A. I. (2025). Thermal denudation landforms in areas of the ice complex occurrence in northern and central Yakutia. *Doklady Earth Sciences*, *525*(3). https://doi.org/10.1134/s1028334x25609551

Kizyakov, A. I., Korotaev, M. V., Wetterich, S., Opel, T., Pravikova, N. V., Fritz, M., Lupachev, A. V., Günther, F., Shepelev, A. G., Syromyatnikov, I. I., Fedorov, A. N., Zimin, M. V., & Grosse, G. (2024). Characterizing Batagay megaslump topography dynamics and matter fluxes at high spatial resolution using a multidisciplinary approach of permafrost field observations, remote sensing and 3D geological modeling. *Geomorphology*, *455*, 109183. https://doi.org/10.1016/j.geomorph.2024.109183

Kizyakov, A. I., Wetterich, S., Günther, F., Opel, T., Jongejans, L. L., Courtin, J., Meyer, H., Shepelev, A. G., Syromyatnikov, I. I., Fedorov, A. N., Zimin, M. V., & Grosse, G. (2022). Landforms and degradation pattern of the Batagay thaw slump, Northeastern Siberia. *Geomorphology*, *420*, 108501. https://doi.org/10.1016/j.geomorph.2022.108501

Kizyakov, A. I., Zimin, M. V., Leibman, M. O., & Pravikova, N. V. (2013). Monitoring of the rate of thermal denudation and thermal abrasion on the western coast of Kolguev Island, using high resolution satellite images. *Earth Cryosphere, XVII*, 36–47. (In Russian)

Kokelj, S. V., Jenkins, R. E., Milburn, D., Burn, C. R., & Snow, N. (2005). The influence of thermokarst disturbance on the water quality of small upland lakes, Mackenzie Delta region, Northwest Territories, Canada. *Permafrost and Periglacial Processes*, *16*(4), 343–353. https://doi.org/10.1002/ppp.536

Kokelj, S. V., Tunnicliffe, J., Lacelle, D., Lantz, T. C., Chine, K. S., & Fraser, R. (2015). Increased precipitation drives mega slump development and destabilization of ice-rich permafrost terrain, northwestern Canada. *Global and Planetary Change, 129*, 56–68. https://doi.org/10.1016/j.gloplacha.2015.02.008

Kunitsky VV, Syromyatnikov II, Schirrmeister L, Skachkov YB, Grosse G, Wetterich S, Grigoriev MN (2013) Ice-rich and thermal denudation in the Batagay area (Yana upland, East Siberia). KriospheraZemli, XVII 1:56–68 (in Russian)

Laaksonen, A. (2022). The Arctic has warmed nearly four times faster than the globe since 1979. *Communications Earth & Environment*, *3*(1). https://doi.org/10.1038/s43247-022-00498-3

Lacelle, D., Brooker, A., Fraser, R. H., & Kokelj, S. V. (2015). Distribution and growth of thaw slumps in the Richardson Mountains–Peel Plateau region, northwestern Canada. *Geomorphology, 235*, 40–51. https://doi.org/10.1016/j.geomorph.2015.01.024

Lafrenière, M. J., Laurin, E., & Lamoureux, S. F. (2013). The impact of snow accumulation on the active layer thermal regime in high Arctic soils. *Vadose Zone Journal*, *12*(1), 1–13. https://doi.org/10.2136/vzj2012.0058

Lamoureux, S. F., & Lafrenière, M. J. (2009). Fluvial impact of extensive active layer detachments, Cape Bounty, Melville Island, Canada. *Arctic Antarctic and Alpine Research*, *41*(1), 59–68. https://doi.org/10.1657/1523-0430-41.1.59

Lantuit, H., & Pollard, W. H. (2005). Temporal stereophotogrammetric analysis of retrogressive thaw slumps on Herschel Island, Yukon Territory. *Natural Hazards and Earth System Sciences, 5*(3), 413–423. https://doi.org/10.5194/nhess-5-413-2005

Leibman, M., Nesterova, N., & Altukhov, M. (2023). Distribution and morphometry of thermocirques in the north of West Siberia, Russia. *Geosciences*, *13*(6), 167. https://doi.org/10.3390/geosciences13060167

Lewkowicz, A. G. (1987). Headwall retreat of ground-ice slumps, Banks Island, Northwest Territories. *Canadian Journal of Earth Sciences, 24*(6), 1077–1085. https://doi.org/10.1139/e87-105

Ling, F., & Zhang, T. (2003). Impact of the timing and duration of seasonal snow cover on the active layer and permafrost in the Alaskan Arctic. *Permafrost and Periglacial Processes*, *14*(2), 141–150. https://doi.org/10.1002/ppp.445

Lozhkin, A., Rivkina, E., Shur, Y., Grosse, G. (2021). Circum-Arctic map of the Yedoma Permafrost Domain. *Frontiers in Earth Science*, *9*. https://doi.org/10.3389/feart.2021.758360

Lupachev, A. V., Tikhonov, A., Tsygankova, V. I., Vasilieva, G. V., & Zanina, O. G. (2017). Preliminary paleoenvironmental analysis of permafrost deposits at Batagaika megaslump, Yana Uplands, northeast Siberia.

Mackay, J. R. (1972). THE WORLD OF UNDERGROUND ICE. *Annals of the Association of American Geographers*, *62*(1), 1–22. https://doi.org/10.1111/j.1467-8306.1972.tb00839.x

Makopoulou, E., Karjalainen, O., Elia, L., Blais-Stevens, A., Lantz, T., Lipovsky, P., Lombardo, L., Nicu, I. C., Rubensdotter, L., Rudy, A. C. A., & Hjort, J. (2024). Retrogressive thaw slump susceptibility in the northern hemisphere permafrost region. *Earth Surface Processes and Landforms*, *49*(11), 3319–3331. https://doi.org/10.1002/esp.5890

Muñoz Sabater, J. (2019): ERA5-Land monthly averaged data from 1950 to present. Copernicus Climate Change Service (C3S) Climate Data Store (CDS). DOI: 10.24381/cds.68d2bb30 (Accessed on 26-MAY -2026)

Murton, J. B., Edwards, M. E., Lozhkin, A. V., Anderson, P. M., Savvinov, G. N., Bakulina, N., Bondarenko, O. V., Cherepanova, M. V., Danilov, P. P., Boeskorov, V., Goslar, T., Grigoriev, S., Gubin, S. V., Korzun, J. A.,

Murton, J. B., et al. (2017). *Preliminary paleoenvironmental analysis of permafrost deposits at Batagaika megaslump, Yana Uplands, northeast Siberia*. *Quaternary Research, 87*(2), 314–330. DOI: 10.1017/qua.2016.15

Nesterova, N. B., Khomutov, A. V., Leibman, M. O., Safonov, T. A., & Belova, N. G. (2021). The inventory of retrogressive thaw slumps (thermocirques) in the north of West Siberia based on 2016–2018 satellite imagery mosaic. *Earth's Cryosphere, 25*. https://doi.org/10.15372/KZ20210604

Nesterova, N., Leibman, M., Kizyakov, A., Lantuit, H., Tarasevich, I., Nitze, I., Veremeeva, A., & Grosse, G. (2024). Review article: Retrogressive thaw slump characteristics and terminology. *The Cryosphere, 18*, 4787–4810. https://doi.org/10.5194/tc-18-4787-2024

Obu, J. (2021). How Much of the Earth's Surface is Underlain by Permafrost? *Journal of Geophysical Research Earth Surface*, *126*(5). https://doi.org/10.1029/2021jf006123

Ohta, T., Hiyama, T., Iijima, Y., Kotani, A., & Maximov, T. C. (2019). Water-Carbon dynamics in eastern Siberia. In *Ecological studies*. https://doi.org/10.1007/978-981-13-6317-7

Opel, T., et al. (2026). *Geochronology of the Upper Ice Complex (Yedoma) exposed in the Batagay Megaslump, East Siberia*. *Arctic, Antarctic, and Alpine Research, 58*(1). DOI: 10.1080/15230430.2026.2622802

Opel, T., Murton, J. B., Wetterich, S., Meyer, H., Ashastina, K., Günther, F., Grotheer, H., Mollenhauer, G.,

PERIGLACIAL FEATURES, Yedoma: Late Pleistocene Ice-Rich Syngenetic Permafrost of Beringia. In *Elsevier eBooks* (pp. 542–552). https://doi.org/10.1016/b978-0-444-53643-3.00106-0

Porter, C., Morin, P., Howat, I., Noh, M., Bates, B., Peterman, K., Keesey, S., Schlenk, M., Gardiner, J., Tomko, K., Willis, M., Kelleher, C., Cloutier, M., Husby, E., Foga, S., Nakamura, H., Platson, M., Wethington, M., Williamson, C., . . . Bojesen, M. (2018). ArcticDEM, Version 3 [Dataset]. In Harvard Dataverse. https://doi.org/10.7910/dvn/ohhukh

Pražnikar, J. (2016). Particulate matter time-series and Köppen-Geiger climate classes in North America and Europe. *Atmospheric Environment*, *150*, 136–145. https://doi.org/10.1016/j.atmosenv.2016.11.056

*Quaternary Research*, *87*(2), 314–330. https://doi.org/10.1017/qua.2016.15

Rantanen, M., Karpechko, A. Y., Lipponen, A., Nordling, K., Hyvärinen, O., Ruosteenoja, K., Vihma, T., &

Schirrmeister, L., Froese, D., Tumskoy, V., Grosse, G., & Wetterich, S. (2013). PERMAFROST AND

Strauss, J., Laboor, S., Schirrmeister, L., Fedorov, A. N., Fortier, D., Froese, D., Fuchs, M., Günther, F., Grigoriev, M., Harden, J., Hugelius, G., Jongejans, L. L., Kanevskiy, M., Kholodov, A., Kunitsky, V., Kraev, G.,

Timofeev D. A. & Vtyurina E. A. (1983). Terminology of Periglacial Geomorphology [in Russian]

Tumskoy, V. E., Torgovkin, N. V., & Romanis, T. V. (2021). Yakutian therocirques. In *Proceedings of the Annual Conference on the Results of Expedition Research: Relief and Quaternary Deposits of the Arctic, Subarctic and North-West Russia* (Issue 8, pp. 252–257). https://doi.org/10.24412/2687-1092-2021-8-252-257 (In Russian)

United Nations Office for the Coordination of Humanitarian Affairs (OCHA). (2026). Russian Federation administrative boundaries; Common operational dataset (COD-AB). HDX Humanitarian Data Exchange. https://data.humdata.org/dataset/cod-ab-rus

U.S. Geological Survey. (10.04.2026). *Landsat 7 Enhanced Thematic Mapper Plus (ETM+) Collection 2 Level-2 science products* [Dataset]. USGS Earth Explorer. https://earthexplorer.usgs.gov

U.S. Geological Survey. (10.04.2026). *Landsat 8 Operational Land Imager (OLI) Collection 2 Level-2 science products* [Dataset]. USGS Earth Explorer. https://earthexplorer.usgs.gov

Vadakkedath, V., Zawadzki, J., & Przeździecki, K. (2020). Multisensory satellite observations of the expansion of the Batagaika RTS and succession of vegetation in its interior from 1991 to 2018. *Environmental Earth Sciences*, *79*(6). https://doi.org/10.1007/s12665-020-8895-7

Vasil'chuk, Y. K., & Vasil'chuk, A. C. (1997). Radiocarbon dating and oxygen isotope variations in Late Pleistocene Syngenetic Ice-Wedges, Northern Siberia. *Permafrost and Periglacial Processes*, *8*(3), 335–345. https://doi.org/10.1002/(sici)1099-1530(199709)8:3

Wang, B., Paudel, B., & Li, H. (2009). Retrogression characteristics of landslides in fine-grained permafrost soils, Mackenzie Valley, Canada. *Landslides, 6*(2), 121–127.

Wlostowski, A. N., Gooseff, M. N., & Adams, B. J. (2017). Soil moisture controls the thermal habitat of active layer soils in the McMurdo Dry Valleys, Antarctica. *Journal of Geophysical Research: Biogeosciences, 123*(1), 46–59. https://doi.org/10.1002/2017JG004018

Woo, M. (2012). *Permafrost hydrology*. https://doi.org/10.1007/978-3-642-23462-0

Zhang, T. (2005). Influence of the seasonal snow cover on the ground thermal regime: An overview. Reviews of Geophysics, 43(4). https://doi.org/10.1029/2004rg000157

Zhang, T., Heginbottom, J. A., Barry, R. G., & Brown, J. (2000). Further statistics on the distribution of permafrost and ground ice in the Northern Hemisphere1. *Polar Geography*, *24*(2), 126–131. https://doi.org/10.1080/10889370009377692

Zhao, L., G. Cheng, S. Li, X. Zhao, and S. Wang. 2000. Thawing and freezing processes of active layer in Wudaoliang region of Tibetan Plateau. Chinese Science Bulletin, 45: 2181-2187. DOI: 10.1007/bf02886326

Zhigarev. L. A., Thermal Denudation Processes and Deformation Behavior of Thawing Sediments (Nauka, Moscow, 1975) [in Russian].).

Zimov, S. A., Davydov, S. P., Zimova, G. M., Davydova, A. I., Schuur, E. a. G., Dutta, K., & Chapin, F. S. (2006). Permafrost carbon: Stock and decomposability of a globally significant carbon pool. *Geophysical Research Letters*, *33*(20). https://doi.org/10.1029/2006gl027484

# 8 Appendix

*Table A1. Shows the for this study utilized data, its resolution and sources.*

| Data | Data type | Resolution | Reference |
|---|---|---|---|
| Sattelite imagery | Landsat 8, Landsat 7 | 30m | U.S. Geological Survey. (10.04.2026). *Landsat 7 Enhanced Thematic Mapper Plus (ETM+) Collection 2 Level-2 science products* [Dataset]. USGS Earth Explorer. https://earthexplorer.usgs.gov<br>U.S. Geological Survey. (10.04.2026). *Landsat 8 Operational Land Imager (OLI) Collection 2 Level-2 science products* [Dataset]. USGS Earth Explorer. https://earthexplorer.usgs.gov |
| Sattelite imagery | Sentinel 2 | 10m | European Space Agency. (accessed 26.05.2026). Copernicus Data Space *Sentinel-2 Level-2A multispectral imagery.* https://browser.dataspace.copernicus.eu/ |
| Temperature | Verkhoyansk Weather station | monthly mean | Japan Meteorological Agency (JMA). (accessed 26.05.2026) *ClimatView climate normals — Verkhoyansk station (WMO ID: 24266)*. World Climate / TCC. https://ds.data.jma.go.jp/gmd/tcc/tcc/products/climate/climatview/graph_mkhtml_nrm.php?n=24266&m=1 |
| Temperature | ERA5-Land | monthly mean | Muñoz Sabater, J. (2019): ERA5-Land monthly averaged data from 1950 to present. Copernicus Climate Change Service (C3S) Climate Data Store (CDS). DOI: 10.24381/cds.68d2bb30 (Accessed on 26-MAY -2026) |
| Temperature | ERA5-Land | daily mean | Muñoz Sabater, J. (2019): ERA5-Land hourly data from 1950 to present. Copernicus Climate Change Service (C3S) Climate Data Store (CDS). DOI: 10.24381/cds.e2161bac (Accessed on 26-MAY -2026) |
| Precipitation | Verkhoyansk Weather station | monthly sum | Muñoz Sabater, J. (2019): ERA5-Land monthly averaged data from 1950 to present. Copernicus Climate Change Service (C3S) Climate Data Store (CDS). DOI: 10.24381/cds.68d2bb30 (Accessed on 26-MAY -2026) |
| Precipitation | ERA5-Land | monthly sum | Muñoz Sabater, J. (2019): ERA5-Land monthly averaged data from 1950 to present. Copernicus Climate Change Service (C3S) Climate Data Store (CDS). DOI: 10.24381/cds.68d2bb30 (Accessed on 26-MAY -2026) |
| Elevation | DEM | 2m | Porter, C., Morin, P., Howat, I., Noh, M., Bates, B., Peterman, K., Keesey, S., Schlenk, M., Gardiner, J., Tomko, K., Willis, M., Kelleher, C., Cloutier, M., Husby, E., Foga, S., Nakamura, H., Platson, M., Wethington, M., Williamson, C., . . . Bojesen, M. (2018). ArcticDEM, Version 3 [Dataset]. In *Harvard Dataverse*. https://doi.org/10.7910/dvn/ohhukh |
| Administrative Boundaries | Polygon layer | | United Nations Office for the Coordination of Humanitarian Affairs (OCHA). (2026). *Russian Federation administrative boundaries — Common operational dataset (COD-AB).* HDX Humanitarian Data Exchange. https://data.humdata.org/dataset/cod-ab-rus |

*Table A2. Shows Satellite Image (USGS) file name of images used in this study and the year they were taken.*

| **Year** | **Sattelite Image Filename** |
|---|---|
| 1991 | Surface Reflectance_LT05_L2SP_122012_19910813_20200915_02_T1_MTL |
| 1999 | p122r012_7x19990827 |
| 2000 | Surface Reflectance_LE07_L2SP_121012_20000806_20200918_02_T1_MTL |
| 2001 | p120r013_7x20010802 |
| 2002 | Surface Reflectance_LE07_L2SP_121013_20020812_20200916_02_T1_MTL |
| 2003 | Surface Reflectance_LE07_L2SP_121013_20031002_20200916_02_T1_MTL |
| 2004 | Surface Reflectance_LE07_L2SP_121012_20040716_20200915_02_T1_MTL |
| 2005 | Surface Reflectance_LE07_L2SP_121013_20050921_20200914_02_T1_MTL |
| 2006 | Surface Reflectance_LT05_L2SP_121012_20060730_20200831_02_T1_MTL |
| 2007 | Surface Reflectance_LT05_L2SP_121013_20070514_20200830_02_T1_MTL |
| 2008 | Surface Reflectance_LE07_L2SP_121013_20080828_20200913_02_T1_MTL |
| 2009 | Surface Reflectance_LT05_L2SP_120013_20090629_20200827_02_T1_MTL |
| 2010 | Surface Reflectance_LT05_L2SP_120013_20100803_20200824_02_T1_MTL |
| 2011 | Surface Reflectance_LT05_L2SP_122012_20110601_20200822_02_T1_MTL |
| 2012 | Surface Reflectance_LE07_L2SP_122012_20120627_20200909_02_T1_MTL |
| 2013 | Surface Reflectance_LC08_L2SP_120013_20130811_20200912_02_T1_MTL |
| 2014 | Surface Reflectance_LC08_L2SP_120013_20130811_20200912_02_T1_MTL |
| 2015 | Surface Reflectance_LC08_L2SP_121013_20150808_20200908_02_T1_MTL |

*Table A3. Shows Satellite Image (Copernicus) file name of images used in this study and the year they were taken.*

| | |
|---|---|
| 2016 | S2A_MSIL2A_20160815T024552_N0500_R132_T53WMQ_20231002T035024.SAFE (1)\S2A_MSIL2A_20160815T024552_N0500_R132_T53WMQ_20231002T035024 |
| 2017 | S2A_MSIL2A_20170711T024551_N0500_R132_T53WMQ_20230904T140647.SAFE (2)\S2A_MSIL2A_20170711T024551_N0500_R132_T53WMQ_20230904T140647 |
| 2018 | S2A_MSIL2A_20180828T025541_N0500_R032_T53WMR_20230817T063034.SAFE\S2A_MSIL2A_20180828T025541_N0500_R032_T53WMR_20230817T063034 |
| 2019 | S2B_MSIL2A_20190609T025549_N0500_R032_T53WMR_20230629T093058.SAFE\S2B_MSIL2A_20190609T025549_N0500_R032_T53WMR_20230629T093058 |
| 2020 | S2A_MSIL2A_20200621T030551_N0500_R075_T53WMR_20230330T013544.SAFE\S2A_MSIL2A_20200621T030551_N0500_R075_T53WMR_20230330T013544 |
| 2021 | S2A_MSIL2A_20210802T025551_N0500_R032_T53WMR_20230130T042743.SAFE\S2A_MSIL2A_20210802T025551_N0500_R032_T53WMR_20230130T042743 |
| 2022 | S2A_MSIL2A_20220728T025531_N0510_R032_T53WMR_20240710T150244.SAFE\S2A_MSIL2A_20220728T025531_N0510_R032_T53WMR_20240710T150244 |
| 2023 | S2B_MSIL2A_20230628T025529_N0510_R032_T53WMR_20240909T181712.SAFE\S2B_MSIL2A_20230628T025529_N0510_R032_T53WMR_20240909T181712 |
| 2024 | S2C_MSIL2A_20250824T030601_N0511_R075_T53WMR_20250824T053712.SAFE\S2C_MSIL2A_20250824T030601_N0511_R075_T53WMR_20250824T053712 |
| 2025 | S2C_MSIL2A_20250821T025601_N0511_R032_T53WMR_20250821T053615.SAFE (3)\S2C_MSIL2A_20250821T025601_N0511_R032_T53WMR_20250821T053615 |

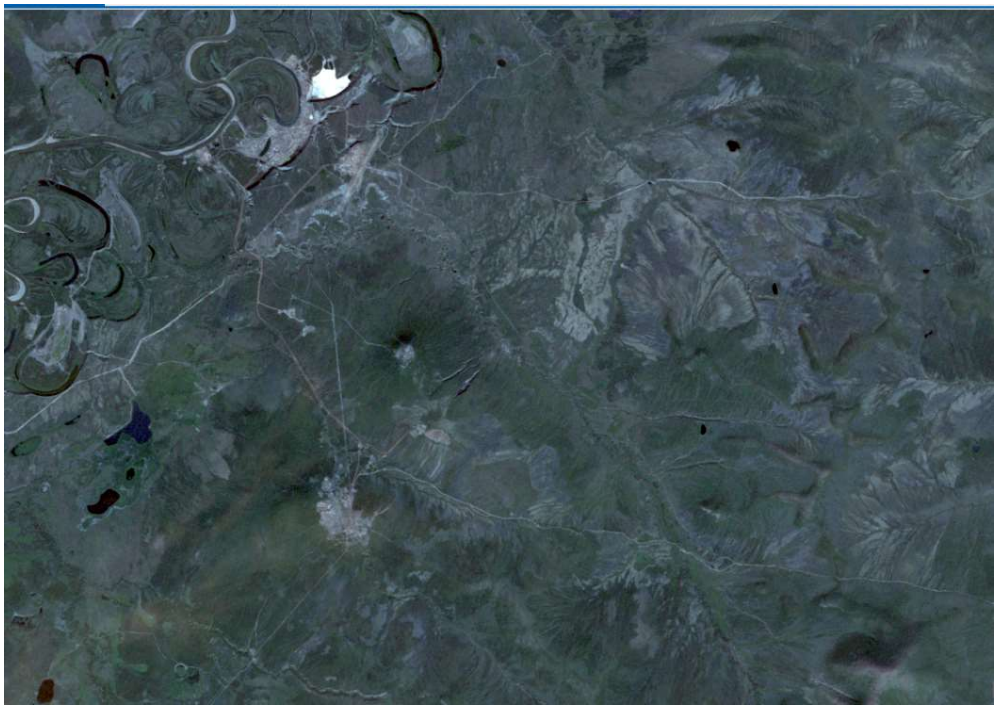

*Figure A1. is a satellite image taken in 1991 (Landsat 8, USGS).*

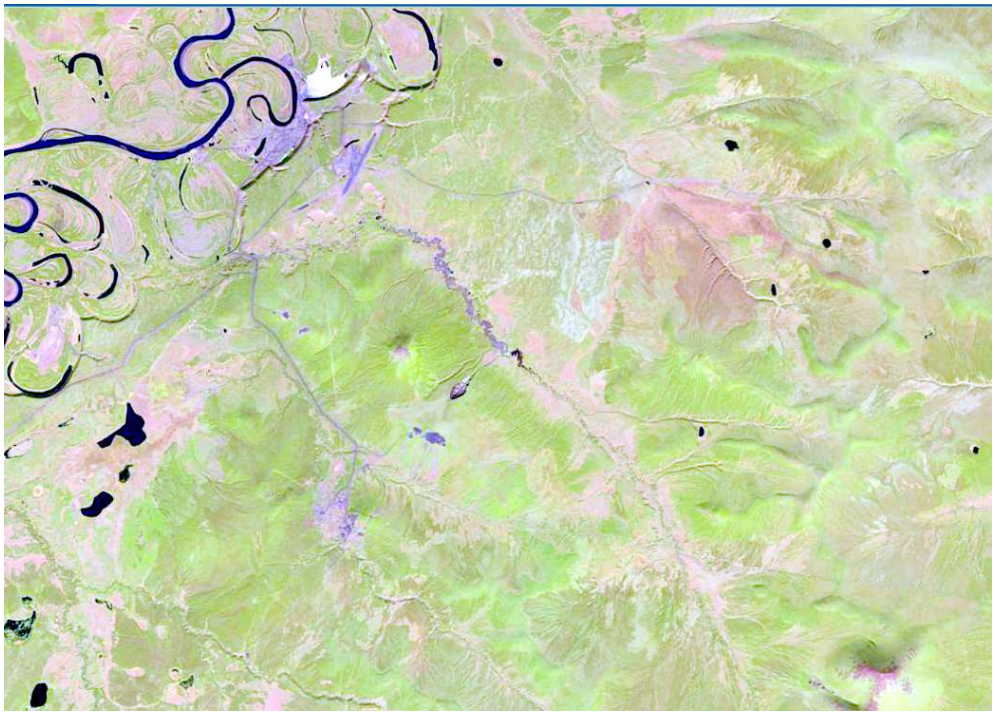

*Figure A2. is a satellite image taken in 1999 (Landsat 8, USGS).*

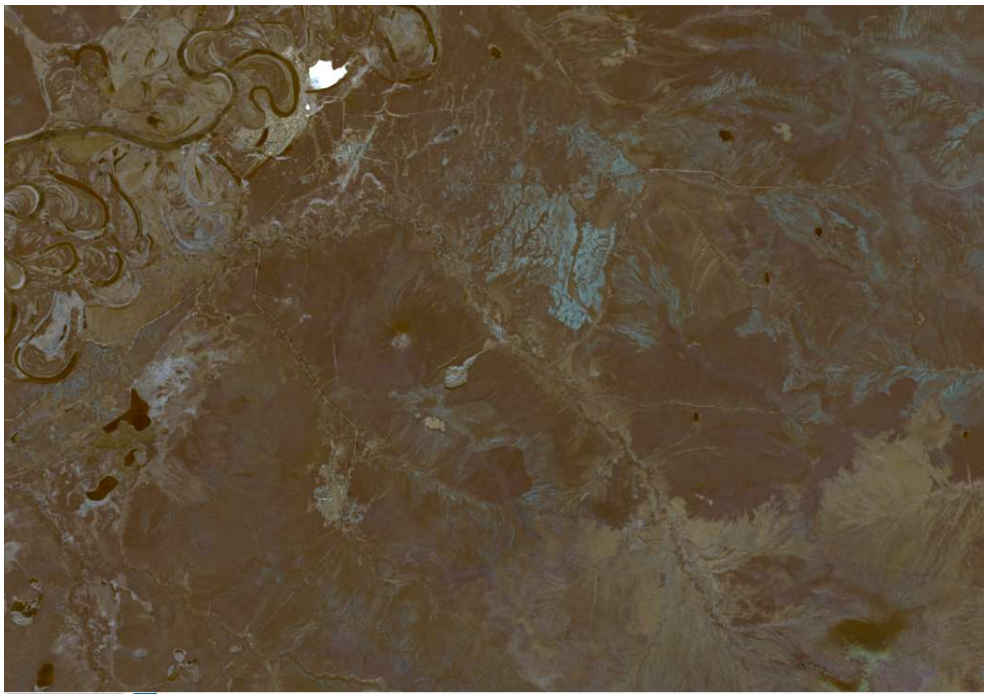

*Figure A3. is a satellite image taken in 2015 (Landsat 8, USGS).*

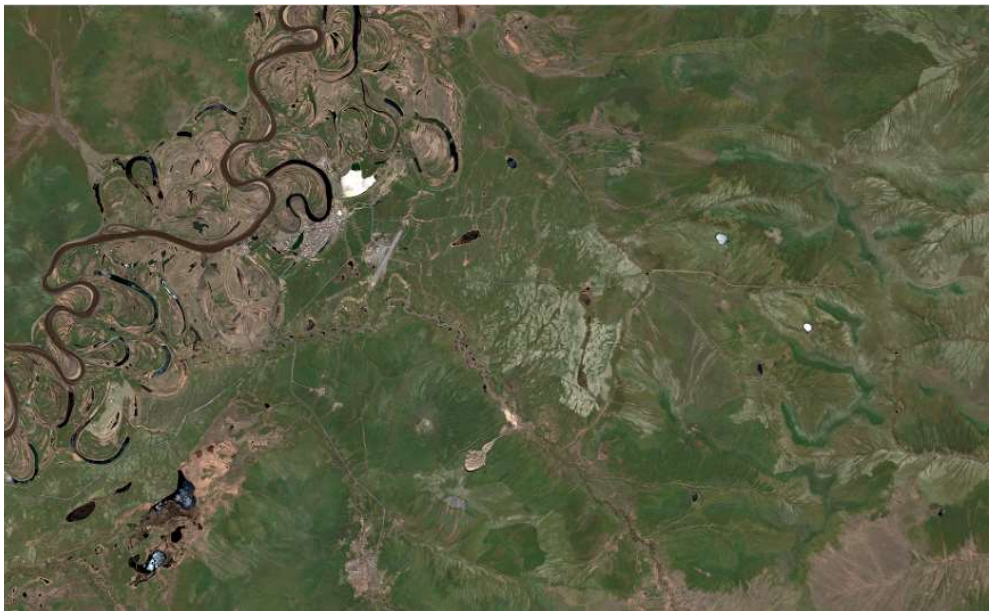

*Figure A4. is a satellite image taken in 2016 (Sentinel-2, Copernicus).*

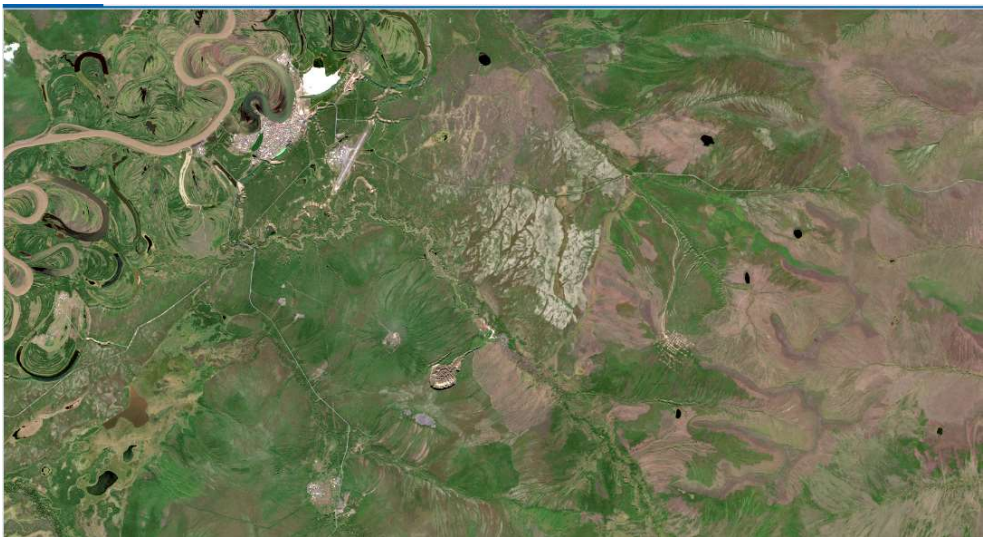

*Figure A5. is a satellite image taken in 2025 (Sentinel-2, Copernicus).*